

# Defect Identification in Organic Photovoltaic Devices Using Thermorelectance Imaging

by  
Liliana Valle  
Professor Janice Hudgings, Advisor



A thesis submitted in partial fulfillment  
of the requirements for the  
Degree of Bachelor of Arts with Honors  
in Physics

POMONA COLLEGE  
Claremont, California  
May 3, 2023

# Abstract

Organic photovoltaics (OPVs) have many potential advantages over inorganic photovoltaic devices, including physical flexibility and ease of mass production. However, widespread adoption of OPVs is limited by lower operating efficiencies and susceptibility to degradation in ambient conditions. In this project, we combine a literature review and the use thermoreflectance imaging, a high-resolution non-contact thermography technique, to locate and explore the physical origins of defects in OPVs. Thermoreflectance images of in-house fabricated, P3HT:PCBM based organic solar cells show strong, localized regions of enhanced reflectivity, indicative of defects. We identify electrical shunts with radial heat spreading associated with the metal contacts, whereas other defects present as concentric rings with no heat spreading, suggesting a potential mechanical origin. This work illustrates the myriad of defects and their signatures, highlighting the utility of thermoreflectance imaging as a tool for identifying and characterizing localized defects in organic solar cells.

# Acknowledgments

First, I would also like to thank the physics senior seminar and Prof. Moreno for providing us with a support system this year. I would also like to highlight the support of my advisor, Prof. Janice Hudgings for giving me valuable advice and feedback during the writing process and for offering me guidance and support throughout my time at Pomona. Similarly, I would like to thank Prof. David Tanenbaum, Sabrina Li, Valerie Wang, Kat Kornegay, and Alfred Molina for access to their resources, fabricating the devices under investigation, and other previous work done for this project. I would be remiss if I did not thank my suitemates of Sontag 260 for putting up with my constant diatribe about my senior projects, and for making the best of this final year at Pomona. Finally, I would like to thank my family, especially my father, Arnoldo for first introducing me to the beauty of physics, Latin food and dance, and for always encouraging me to explore my diverse passions. Chirp chirp!

# Contents

<b>Abstract</b>	i
<b>Acknowledgments</b>	ii
<b>1 Introduction</b>	1
1.1 Motivation . . . . .	1
1.2 Relevant photovoltaic technologies . . . . .	3
1.2.1 First and second generations . . . . .	3
1.2.2 Emergent Technologies . . . . .	4
1.3 Research Objectives . . . . .	5
<b>2 Theory</b>	6
2.1 Inorganic photovoltaics . . . . .	6
2.1.1 Materials and structure . . . . .	6
2.1.2 Doping and biasing p-n junctions . . . . .	7
2.1.3 Photon absorption and power generation . . . . .	8
2.2 Organic photovoltaics . . . . .	9
2.2.1 Differences from inorganic semiconductors . . . . .	9
2.2.2 Materials and structure . . . . .	9
2.2.3 Device architectures . . . . .	10
2.2.4 Photoelectric energy conversion . . . . .	11
2.3 Device performance metrics . . . . .	13
2.3.1 <i>IV</i> characteristics . . . . .	13
2.3.2 Open circuit voltage and short circuit current . . . . .	14
2.3.3 Fill factor . . . . .	14
2.3.4 Power conversion efficiency . . . . .	14
<b>3 Methods</b>	16
3.1 Experimental Devices . . . . .	16
3.1.1 P3HT:PCBM cells . . . . .	16
3.2 Chip mount . . . . .	17
3.3 <i>IV</i> curve setup . . . . .	18
3.4 Imaging techniques . . . . .	20

3.4.1	Fluorescence microscopy . . . . .	20
3.4.2	Light beam induced current (LBIC) . . . . .	21
3.4.3	Thermal imaging . . . . .	23
3.5	Thermoreflectance imaging system . . . . .	23
3.5.1	Amplitude and Phase maps . . . . .	25
<b>4</b>	<b>Characterizing defects</b>	<b>28</b>
4.1	Defect origins . . . . .	28
4.1.1	Crystallization . . . . .	28
4.1.2	Fabrication mechanisms . . . . .	29
4.2	Defect types . . . . .	30
4.2.1	Shunts . . . . .	30
4.2.2	Trap states . . . . .	30
4.2.3	Chemical impurities . . . . .	32
4.2.4	Structural alterations . . . . .	33
4.2.5	Fabrication Shunts . . . . .	36
4.2.6	Material Shunts . . . . .	39
4.3	Defect prevention . . . . .	41
<b>5</b>	<b>Progress and Conclusion</b>	<b>42</b>
5.1	Experimental data . . . . .	42
5.1.1	IV curves . . . . .	42
5.1.2	Thermoreflectance images . . . . .	42
5.2	Research progress . . . . .	44
5.3	Future of OPVs . . . . .	50

# List of Figures

1.1	National Renewable Energy Lab cell efficiencies over time. From [1] . . . . .	2
1.2	Mono-crystalline Solar Cells [2] . . . . .	3
1.3	Poly-crystalline Solar Cell from [3] . . . . .	4
2.1	Typical band structures in insulators, conductors, and semiconductors. From [4] . . . . .	6
2.2	When N-type (right) and P-type (left) materials are placed next to each other, a p-n junction is formed. A depletion region is generated at the interface of the materials due to the generation of an electric field. From [5] . . . . .	7
2.3	Schematic demonstrating the movements of charge carriers under (a) forward biases and (b) reverse biases. From [6] . . . . .	8
2.4	Bilayer cell (left) Bulk heterojunction cell (right) [7] . . . . .	10
2.5	Energy level diagram illustrating the photoelectric conversion mechanism. The numbered processes are as follows: 1. Photon absorption in the acceptor region and exciton generation, 2. Exciton diffusion, 3. Exciton dissociation, 4. Charge carrier transport and 5. Charge carrier collection. The band gaps are depicted as the filled in rectangle from the electron transport layer to hole transport layer. The top of the cathode and anode depict the work function. From [8]. . . . .	11
2.6	<i>IV</i> curve for a solar cell under dark and illuminated conditions. $V_{OC}$ represent the maximum voltage that can be obtained from a solar cell when there is no current flowing through while $I_{SC}$ represents the largest amount of current that can be extracted, and the current flowing through the cell when the voltage across it is zero. $I_{mp}$ and $V_{mp}$ are the current and voltage the cell should be operated at to attain its maximum power output. From [7]. . . . .	13
2.7	Graphical representation of the fill factor for a solar cell. <i>IV</i> curve "squareness" relating actual output to the theoretical (left). Two <i>IV</i> curves demonstrating high and low fill factors. From [7]. . . . .	15
3.1	Layering of applied materials of P3HT:PCBM cells [9] . . . . .	16
3.2	Cross section of P3HT:PCBM in-house cells. . . . .	17
3.3	Mobile magnetic plate setup. The cell is probed at the contacts to be characterized either by IV curves or Thermoreflectance imaging. . . . .	18

3.4 Sunbrick solar simulator with mobile magnetic mount under illumination. . . . .	19
3.5 Fluorescence microscopy of two poly-Si solar cells. Bare cell (left), bare pc-Si solar cell with concentric circles indicating a region of $\times 10$ higher microscopy (middle), Coated sample with PA Si-QDs (right). The arrows indicate the position of a silver finger. From [10] . . . . .	20
3.6 An EL image of a multicrystalline solar module exhibiting two large cracks. From [11] . . . . .	21
3.7 PL image of a six-inch SiN multicrystalline silicon wafer demonstrating effective minority carrier lifetime. Attained megapixel resolution in $< 1$ s. From [12] . . . . .	21
3.8 LBIC images of a thin-film CIGS solar cell. Dark red represents the maximum photocurrent of 102 micro amps. Map A was measured with 10 micro meter steps, while map B uses 4 micro meter steps. Map B presents a higher resolution, indicated by the 10 micro meter wide contact finger (vertical black line). [13] . . . . .	22
3.9 Internal quantum efficiency measurements of a solar cell at four different wavelengths. From [14] . . . . .	22
3.10 Dark lock-in thermography image of a silicon solar cell. Breakdowns are indicated by the red regions of higher temperature (left) From [15]. TR image of a 9x9mm region of an organic solar cell. Brighter coloring indicates greater relative heating to the rest of the cell. (right) . . . . .	23
3.11 Schematic of the thermoreflectance imaging system. From [16] . . . . .	24
3.12 Plot of Thermoreflectance signal over one and a quarter modulation periods. From [16] . . . . .	25
3.13 From $\Delta R/R$ and $\phi$ images of a commercial Evergreen silicon solar cell. From [17] . . . . .	27
4.1 Introduction of defects in the crystal structure of a solar cell.(a) Ideal crystal structure without defects; (b) after defect introduction; (c) point defects;(d) paired defects; and (e) widespread defects. Adapted from [18] . . . . .	29
4.2 Potential charge recombination pathways in semiconductors. (a)"Band-to-Band," a radiative process involving transition of excited electrons at the CBM back to the ground state to recombine with holes at the VBM, (b) Shallow-level trap, (c) Deep-level trap exhibiting non-radiative recombination, (d) "Band-to-Band" recombination where no defects are present, (e) Shallow-level defect radiative recombination, and (f) Deep-level defect non-radiative recombination. Adapted from [18] . . . . .	31
4.3 Conceptual illustration of the density of states in an OPV. From [7] . . . . .	31
4.4 Classifications of chemical intrusions in monocrystalline silicon cells. From [19]	34
4.5 A SEM image of a dark grain boundary. Carbon and oxygen precipitates and voids can be observed. From [20] . . . . .	34

4.6 LBIC scan of an RGS silicon wafer over an optical microscopy image. Defective regions are highlighted in white rectangles, the black rectangle signifying a patterned region of current collection. From [20] . . . . .	36
4.7 EL image of a polycrystalline solar cell(left) Focused images of three large defect clusters A, B, and C (right). From [21] . . . . .	36
4.8 Lock-in thermogram of a 10x10 cm sq multicrystalline silicon solar cell under forward bias. Edge shunt mostly visible in the upper right hand region. From [22] . . . . .	37
4.9 Lock-in thermogram of a similar multicrystalline silicon cell with two scratches that induced shunts. From [23] . . . . .	37
4.10 SEM image of a "hump" in the structure of a thin-film polycrystalline silicon cell on a substrate exhibiting shunting when covered by the emitter grid. From [22] . . . . .	38
4.11 An EL image (left) and a thermal image (right) of linear ohmic shunts in a thin-film aluminum-silicon solar cell. From [24] . . . . .	38
4.12 Lock-in thermogram of a multicrystalline silicon cell with shunting caused by an intrusion of Si3N4. From [23] . . . . .	39
4.13 (a) Lock-in thermogram; (b) EBIC image; and (c) TEM image of a multicrystalline silicon cell shunting due to strongly recombinative crystal defects [23]	40
4.14 Thermography images of reverse biased multicrystalline cells under a periodically applied bias current of -1.6 A. The red spot in the upper right hand corner characterizes a local shunt (left) and the uniform temperature distribution signifies no shunting activity (right). From [25] . . . . .	40
5.1 Bulk <i>IV</i> curve of an in-house fabricated device from 2019 using a solar simulator with incoming power $100\text{mW}/\text{cm}^2$ under dark and light conditions. The graphed cell exhibits efficiencies up to $\eta = 3\%$ . . . . .	43
5.2 Bulk <i>IV</i> curve of an in-house fabricated device using a Sunbrick solar simulator with incoming power of 1 sun ( $1000\text{ W/m}^2$ ) under dark and light conditions. The cell exhibits efficiencies $\eta = 0.02 - 3\%$ . . . . .	43
5.3 TR amplitude $\Delta R/R$ (a) and (b) phase $\Phi$ of a hot spot and three scratches in the active region of an in-house fabricated cell taken by previous Hudgings lab students [16] . . . . .	45
5.4 (a) $\Delta R/R$ image of a radially symmetric hot spot in the active region of in-house fabricated cell (b) $\Delta R/R$ plotted against squared voltage modulation amplitude [ $\Delta V^2$ ] of the hot spot in (a) demonstrating a linear relationship.(c) $\Delta R/R$ plotted against the radial distance in pixels demonstrating heat spreading radially away from the center of the defect. Taken by previous Hudgings lab students. [7] . . . . .	46
5.5 Radial hot spots in a silicon solar cell that scale inversely with modulation frequency. Shunts were cited to be caused by an open emitter from fabrication errors. [26] . . . . .	47

5.6 (a) $\Delta R/R$ image of an in-house fabricated cell with a defect signature comprised of concentric rings, (b) and (c) present plots of $\Delta R/R$ against radial distance, demonstrating the decreasing thermal signature as the radial distance increases. Taken by previous Hudgings lab students.[7] . . . . .	48
5.7 Photoluminescence image of a concentric ring defect on Czochralski-grown silicon wafers. Further imaging revealed the presence of oxygen impurities on the cell surface.[27] . . . . .	49
5.8 Electroluminescence image of a ring or "doughnut" defect on Copper indium gallium selenide cell. This imaging method measure the luminescence of the cell, demonstrating a recombinative defect as a resulting in photon emission. [28] . . . . .	49

# Chapter 1

## Introduction

This chapter lays out the motivation for this project, highlighting a brief history of solar technologies that lead to a discussion of the devices used in this research. Finally, the objectives of this investigation are mentioned, combining a literature review with experimental results to yield a complete understanding of the direction of organic technologies.

### 1.1 Motivation

The potential of solar technology was first realized in 1955 with the creation of the solar cell from Bell Laboratories to attempt to power telecommunication systems [29]. While the original technologies only functioned to serve space crafts, the device consisted of "modules" or groups of nine cells encapsulated in silicone oil fit inside of a plastic case then placed in an aluminum case under a glass sheet. These modules generated around 10W of power per day with maximum efficiencies at around 2 percent [30]. Similar modules began to develop use around the world with notable increases in efficiency made in Japan by Sharp Technologies to around 4-5 percent [30]. With inconsistencies in oil supply from the Middle East in the 1970s and 80s, the threat of a power crisis in the United States propelled start-up companies to invest in developing solar technology. In 1973 the Solar Power Corporation developed a module of five cells mounted in a glass-reinforced circuit board covered with silicone rubber that maxed out efficiencies at 5-6 percent [30]. The low but increasing efficiencies, coupled with the inability to ward off wildlife and resist the elements of weather pushed both US and global developments in solar technology [29].

As solar technologies continue to develop in the face of pressing energy concerns as a response to climate change, improving device performance by increasing efficiencies and identifying defects has become a central concern. In order to reliably evaluate device performance, research that uses a suite of imaging characterization techniques has been developed to identify defects. As the body of defect literature grows, this project seeks to add by characterizing the developing Organic Photovoltaic (OPVs) technology against the traditional widely commercialized silicon solar cells.

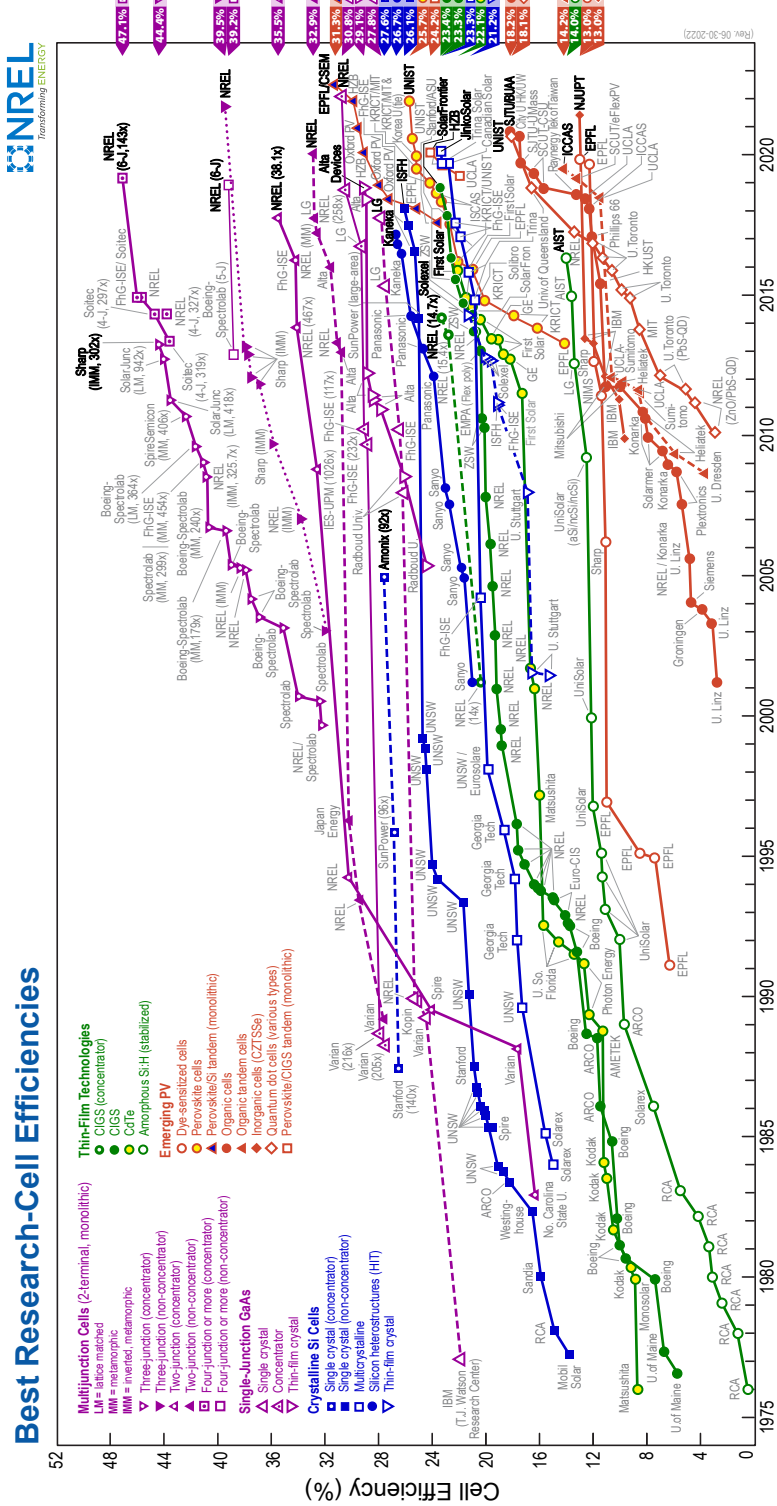


Figure 1.1: National Renewable Energy Lab cell efficiencies over time. From [1]

## 1.2 Relevant photovoltaic technologies

Solar technologies have developed substantially since their inception. Over time, their advancements have been classed into sequential families of technologies. The initial solar cells fall under the first generation of wafer-based silicon technologies, followed by the second generation of thin-film. Finally, research in recent years has yielded a third generation of emergent technologies that consist of many types including Organic Photovoltaics (OPVs) that this project investigates. The development of the efficiencies of these technologies can be viewed in Fig. 1.1.

### 1.2.1 First and second generations

#### Wafer-Based Technologies

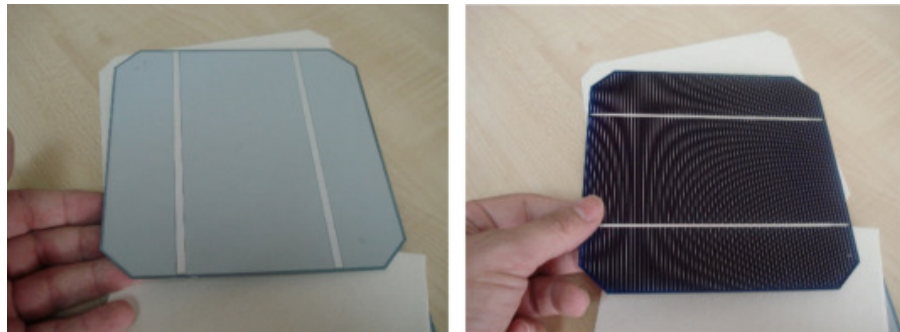


Figure 1.2: Mono-crystalline Solar Cells [2]

The first generation of solar cells is composed of mono-crystalline and poly-crystalline or multicrystalline silicon cells. Mono-crystalline cells consist of a single crystal base of silicon that defines the wafer which can be viewed in Fig. 1.2. The initial cells boasted efficiencies of 12-16 percent that have increased to around 28 percent with refined production methods and further research [2]. However, the wafer base accounts for more than half of production costs, leading to a preference for the multi-crystalline structure over the single wafer.

Poly-crystalline silicon cells are produced from the solidification of molten silicon which grows multiple crystals as opposed to a single crystal from pure silicon exhibited by mono-crystalline cells as can be seen in Fig. 1.3. While this method of production is significantly cheaper than that of mono-crystalline cells, the uneven crystal growth and distribution lower efficiencies from mono-crystalline cells to around 23 percent [3].

#### Thin-Film Technologies

The second generation evolved to include multiple materials including amorphous silicon, cadmium telluride, cadmium indium selenide, and other similar compounds [31]. The thin-film technologies signal an improvement over the wafer base through lower production costs

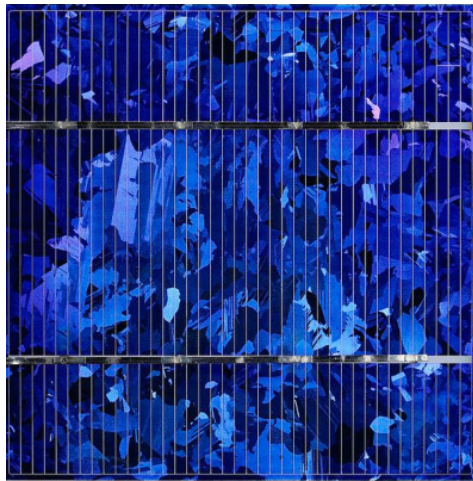


Figure 1.3: Poly-crystalline Solar Cell from [3]

and a flexible substrate. The flexible substrate paves the way for newer technology to be developed for mass production and applications in other fields. Still, amorphous silicon thin-films present unreliable efficiencies while others such as cadmium telluride contain highly toxic rare earth metals which have pushed developments in solar technologies in new directions [32].

### 1.2.2 Emergent Technologies

#### Perovskites

Perovskite solar cells are an emergent solar technology that has attracted much attention and research in recent years. Their name describes their general chemical structure,  $ABX_3$ , where A and B refer to a large and small organic cation respectively, and X is a halogen anion [33]. This structure features many qualities of traditional silicon cells such as high carrier mobility, while offering the advantages of accessible material and cheap manufacture from organic technologies. Pure perovskite is comprised of calcium, titanium, and oxygen but their characteristics vary depending on the quantity of each atom that are present.

Due to the relative accessibility of their component chemicals, perovskites have become an attractive candidate for the future solar cell market. As of 2016 perovskites have become the fastest advancing solar technology, bringing their efficiencies from 3.8 percent to 25.7 percent in 2021 [33]. Still, the short and long term stability of perovskites challenges their mass application and begs for further investigation.

#### Organic Photovoltaics (OPVs)

OPVs are an emerging solar cell technology that presents many potential advances in production and efficiency for the mass market. Their biggest promise lies in the diversity of

organic materials that can be used in their construction that mitigate previous toxicity concerns and dramatically lower production costs [29]. Still, current efficiencies are lower than previous generations of solar technology and research is still being developed in order to better scale to mass production and increase their lifetime.

OPVs are made with active layers that exhibit organic semiconductors in two forms; small molecules and conjugated polymers that aid in light absorption and distributing charge carriers [8]. They are often fabricated using roll-to-roll printing techniques under ambient conditions that favor large-scale production and low costs. These techniques also favor a flexible substrate similar to thin-films that broaden their applications outside of traditional power sources.

While many qualities of OPVs favor their success in the mass market, current production quantities and efficiencies do not compete with earlier generations of solar technologies. In order to accelerate the evolution of this promising technology, this project focuses its investigation on characterizing defects caused by mechanical and environmental stressors. This research hopes to contribute to the effort to increase OPV efficiencies to more competitive levels of previous generations as can be seen in Fig. 1.1.

### 1.3 Research Objectives

Building upon the years of research done by Pomona students in the Hudgings Lab, this project seeks to understand the mechanisms driving defects in some of the most cutting-edge solar cell technology discussed in this chapter, Organic Photovoltaics (OPVs). The goal is to characterize the defects in OPV devices through a thermoreflectance imaging technique along with comparison to previously characterized defects in the literature. The thermoreflectance imaging technique aims to yield other quantitative information about the thermal signatures of the cells to aid in determining the origins of the defects. The literature review in combination with the experimental results yields a greater understanding of the range of defects found in solar cells, and how research can progress to prevent their origins.

The results of this project are compared to signatures and defects from other imaging techniques found in the literature to yield a greater understanding of the physical mechanisms driving defect formation. The application of these results will in turn drive the improvement of OPV and solar cell technology to provide a more reliable and efficient energy source.

# Chapter 2

## Theory

This chapter outlines the structures and principles involved in the operation of both inorganic and organic solar devices and subsequently introduces standard metrics that characterize device performance relevant to this research.

### 2.1 Inorganic photovoltaics

In order to understand the functionality of emergent technologies that this project focuses on such as OPVs, we start with a foundational understanding of inorganic device types.

#### 2.1.1 Materials and structure

Inorganic semiconductors are comprised of elements from groups 3-5 of the periodic table. In particular, Silicon from group 4 appears in crystalline and amorphous forms, as detailed in the previous chapter. Silicon is advantageous as its band structure, or range of energies that its electrons may have, promotes charge conduction [34].

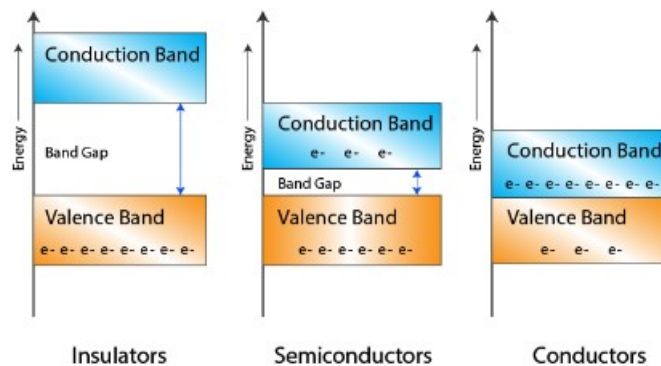


Figure 2.1: Typical band structures in insulators, conductors, and semiconductors. From [4]

Charge conduction occurs when electrons gain enough energy to move across the band gap from the valence band to the conduction band. The band gap energy is the minimum required to excite an electron from the valence to the conduction band. Once electrons in the valence band are excited at this energy, they move to the conduction band, conducting charge and generating current for the solar cell [34]. The band gap varies by material, permitting the existence of various materials displayed in Fig. 2.1. Conductors are materials with no band gap, allowing charge to be conducted freely. Insulators are materials with large band gaps to inhibit charge conduction, and semiconductors consist of band gaps lie in between.

### 2.1.2 Doping and biasing p-n junctions

Doping refers to the process of adding elemental impurities to raise a material's original conductivity. There are two types of doping that are relevant to solar cells: p and n types. N types come from group 5 of periodic table while P types come from group 3. To create these doped materials, atoms from the given elemental group are placed in a silicon lattice, replacing a number of silicon atoms. Because of their differing amounts of valence electrons, holes are the primary charge carrier in p-type materials, while electrons are in n-type materials [32]. When p-type and n-type materials are placed next to each other, a p-n junction,

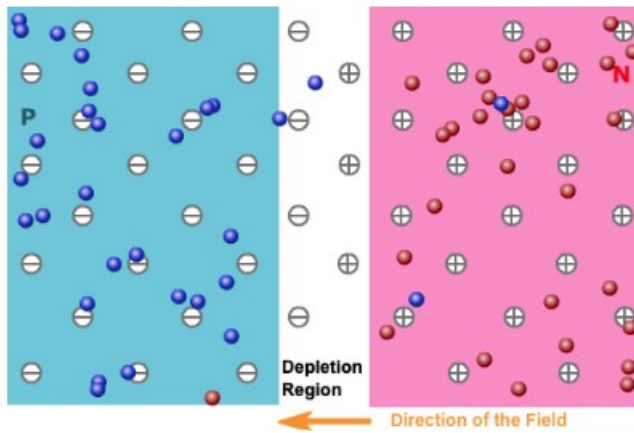


Figure 2.2: When N-type (right) and P-type (left) materials are placed next to each other, a p-n junction is formed. A depletion region is generated at the interface of the materials due to the generation of an electric field. From [5]

also commonly called an emitter in silicon solar cells, is formed. Free electrons in the n-type region will travel to the p-type region, with holes in the p-type region travelling to the n-type region due to each concentration gradient. One might expect this diffusion to occur until their relative concentrations became equal across the device, however, because holes and electrons carry charge, they leave behind exposed ion cores that alter the relative charges of the regions as one moves towards the center of a given region. This activity generates an electric field, thus limiting the movement of electrons and holes effectively generating a depletion region at the junction where this activity occurs [32].

As previously discussed, charges move across the junction regardless of the application of an electric field. To understand the movement of charges with bias, we can define diffusion and drift currents. Diffusion currents correspond to the movement of majority carriers due to the presence of a concentration gradient. Drift currents describe the movement of minority carriers across the depletion region to the region of majority concentration as a response to the electric field which can be understood in Fig. 2.2[6].

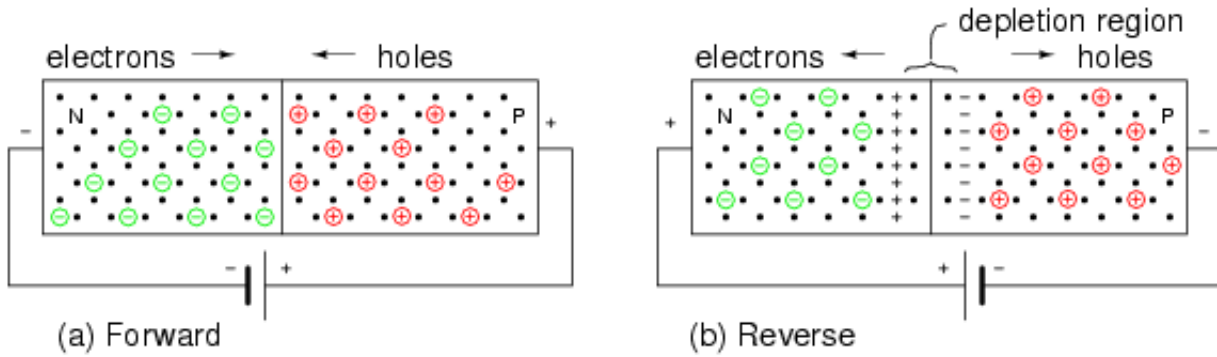


Figure 2.3: Schematic demonstrating the movements of charge carriers under (a) forward biases and (b) reverse biases. From [6]

Under forward biases, the p-side of the junction remains positive, the n-side negative, generating a competing electric field to the existing field. As the original field weakens, majority carriers (electrons in n-type, holes in p-type) can diffuse more easily, lowering the drift current, allowing the diffusion current to increase. This relationship is demonstrated in Fig. 2.3 (a).

Under reverse biases, the opposite process occurs. The p-side of the junction retains a negative voltage with the n-side at a positive voltage seen in Fig. 2.3 (b). As a response, the original electric field is strengthened, increasing the drift current while lowering the diffusion current. At large enough reverse biases, the breakdown voltage of a diode can be reached, however they are not relevant to this discussion.

### 2.1.3 Photon absorption and power generation

In order to contribute to power generation in a solar cell photons incident on the cell surface must be absorbed. However, as incident photons comprise a range of energies, they can also be reflected or transmitted; such processes are considered energy losses to be limited.

The energy of an incident photon determines how it will interact with the cell. If the incident energy is less than the band gap energy, then the photon will be transmitted. If the energy is equal or greater than the band gap energy, then the photon is absorbed. However, when the energy is greater the photons are strongly absorbed, releasing heat and an extra electron to harness the appropriate energy to generate current through and voltage across cell under operating conditions [32].

In order for solar cells to produce power, current and voltage must be generated by the device in accordance with the electrical power equation  $P = IV$ . When incident photons are absorbed, electron-hole pair production on either side of the p-n junction increases the concentration of minority charge carriers on each side [32].

If the minority charge carriers are caught by the electric field in the depletion region before charge recombination, then the field will sweep them to the side of their majority concentration, increasing the drift or reverse current in the diode. Meaning, when charges accumulate on each side of the junction with the separation maintained by the electric field in the depletion region, a voltage is built across the device. If the device terminals are connected to an external circuit, reverse current can flow out from the p-side terminal to the n-side terminal, allowing for power extraction from the device under light [32].

## 2.2 Organic photovoltaics

### 2.2.1 Differences from inorganic semiconductors

While inorganics and OPVs share many analogous qualities, their differences determine their respective performance and applications. Charge carrier transport and mobility mechanisms differ in organics as carriers must move through the disordered conjugated polymers by "hopping" from one site to another, with each "hop" requiring an activation energy. Thus, OSCs suffer from lower carrier mobilities. However, OSCs maintain higher absorption coefficients as opposed to their inorganic counterparts, affording thinner active layers for OPVs [34]. Similarly, the OSC polymers are bonded through weak interactions which permits their flexibility over the rigidity of inorganics. In a future section the photoelectric energy conversion mechanism is discussed. In this process, excitons - a bound state of an electron and a hole attracted through the Coulomb force - are formed. Their formation processes in OPVs is different as they form more easily due to the more compatible weak chemical bonding structure while inorganics exhibit stronger covalent bonds. Excitons also dissociate less easily in OPVs due to similar bonding structures, which is important when drawing current from the cell, and is partially responsible for OPV degradation over time [35]. While many more divergences between organics and inorganics exist, those mentioned above maintain the most relevance to this thesis.

### 2.2.2 Materials and structure

Distinct from inorganics, OPVs rely on the structure of organic semiconductors (OSCs) to perform photoelectric energy conversion. Organic semiconducting polymers consist of long chains of carbon that alternate between single and double bonds between atoms. The chain is termed a conjugated system, enabling its distinct conductive properties. Such a structure yields two characteristics of interest when evaluating OPVs; the highest occupied molecular orbital (HOMO), and lowest unoccupied molecular orbital (LUMO) [34].

The equivalent to valence and conduction bands in inorganics, HOMO and LUMO are important energy levels in understanding band structure and the bonding and anti-bonding energies of OSCs. The difference between the lowest energy of the HOMO and the highest energy of the LUMO is equivalent to the band gap energy found in inorganics, with OPVs exciting electrons from the HOMO to the LUMO [34].

### 2.2.3 Device architectures

The most basic OPV structure is a bilayer cell, shown in Fig. 2.4. The bilayer consists of a cathode and anode as bookends to the acceptor and donor materials. Donor material consists of carbon-based polymers or molecules that absorb sunlight and transfer electrons to the acceptor material. The acceptor material, takes electrons from the donor and transports them to the cathode [32]. The acceptor and donor materials share the same plane to comprise the active layer of the cell. The planar interface limits the efficiency of exciton dissociation by forcing absorbed excitons to pass through the acceptor layer prior to reaching the acceptor/donor interface to separate. Thus, compromises can be made when concerning the thickness of the active layer with thicker layer affording the absorption of more photons, but lower dissociation efficiencies [32]. The mechanics of the photoelectric energy conversion process are further discussed in the following section.

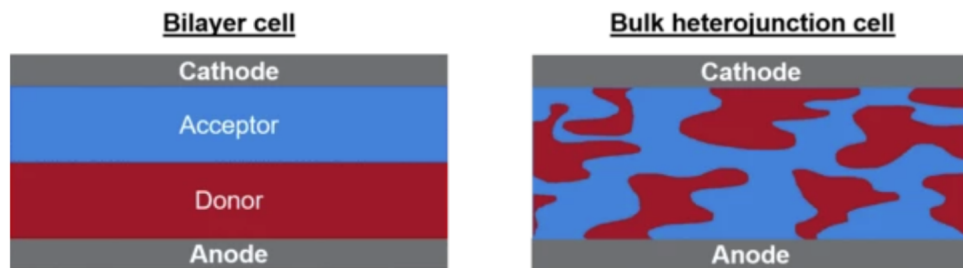


Figure 2.4: Bilayer cell (left) Bulk heterojunction cell (right) [7]

Research in OPV structures have prompted breakthroughs in their efficiencies, leading them to more comparable levels with earlier inorganic generations of devices. Most notably, the development of a bulk heterojunction active layer has permitted higher efficiencies than all previous structures. The bulk heterojunction technique consists of acceptor and donor materials mixed in solution to the nano-scale prior to application to the substrate. The solution permits a thicker active layer while shortening diffusion lengths, conserving exciton dissociation efficiencies. Still, the ability to precisely replicate the mixture of the solution continues to limit OPV efficiencies.

### 2.2.4 Photoelectric energy conversion

The energy conversion mechanism in OPVs occurs in four principal steps: photon absorption and exciton generation; exciton diffusion; exciton dissociation; and carrier transport and collection which can be understood in Fig. 2.5.

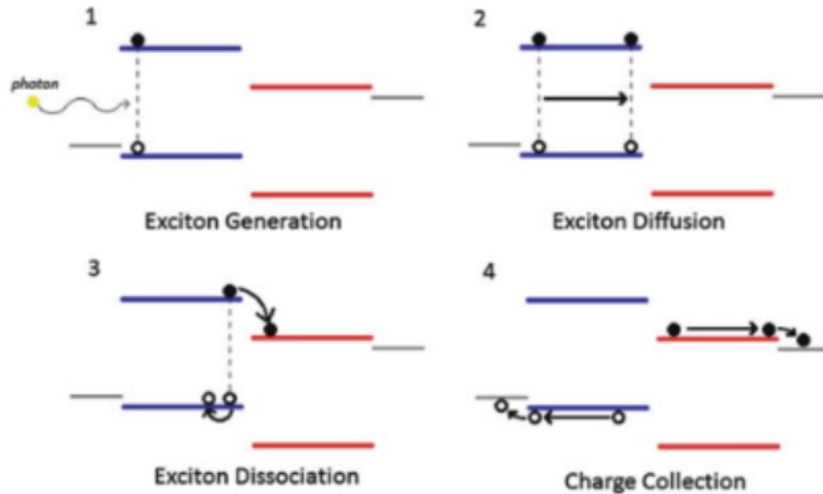


Figure 2.5: Energy level diagram illustrating the photoelectric conversion mechanism. The numbered processes are as follows: 1. Photon absorption in the acceptor region and exciton generation, 2. Exciton diffusion, 3. Exciton dissociation, 4. Charge carrier transport and 5. Charge carrier collection. The band gaps are depicted as the filled in rectangle from the electron transport layer to hole transport layer. The top of the cathode and anode depict the work function. From [8].

#### Photon absorption and exciton generation

When the energy of an incident photon is greater than the material's band gap energy and is subsequently absorbed, a Frenkel exciton is produced in the OSC, similarly to inorganics. Excitons represent the bound state between an electron and hole, and are packets of energy confined within a material that mediates the conversion of sunlight into electrical energy in solar cells [35]. However, in OSCs the exciton does not have sufficient energy to dissociate at room temperature, requiring it to survive long enough to diffuse to an interface where it can separate.

#### Exciton diffusion

Exciton diffusion through the OSC towards the separation interface is defined by its diffusion length  $L_D$ , or the average distance the exciton can travel between generation and recombination. The diffusion coefficient  $D$  describes the rate of the exciton's movement, and

the diffusion lifetime  $\tau$  that characterizes the amount of time the exciton can persist before recombination. If recombination occurs, the excess energy will be released as a photon [35]. The quantities can be related through the following

$$L_D = \sqrt{D\tau} \quad (2.1)$$

### Exciton dissociation

Exciton dissociation occurs at the heterojunction interface, or where two OSCs with aligned energy bands meet. The heterojunction, previously described in section 2.2.3, is comprised of the donor and acceptor materials the active layer of the cell as seen in Fig. 2.4. The donor and acceptor materials are chosen to be electron-rich and electron-deficient respectively [35].

Separation occurs when the LUMO of the donor material is higher than LUMO of acceptor material, following that the same conditions are met for the HOMO. At the separation interface, the difference between the HOMO and LUMO of the acceptor material must be less than the potential energy of the electron-hole pair such that when the exciton arrives at the heterojunction, it becomes permissible for the electron to move through from the LUMO donor to acceptor. The movement of the electron leaves a hole on the HOMO donor, indicating a charge movement across the interface [16].

Charge separation must follow this process as the electron-hole pair remain Coulombically attracted and still subject to recombination. This is described in the following section.

### Carrier transport and collection

In order to understand carrier transport it becomes necessary to revisit our understanding of drift and diffusion currents. Diffusion currents describe the movement of charge carriers down the concentration gradient while drift current characterize the response of charge carriers to an electric field [8].

When external voltage bias is applied to the cell, the electric field can be manipulated, affecting both types of currents. Naturally, when electric field is strong in one direction, so is the drift current as minority charge carrier are swept to a given side of the boundary. Conversely, when the field is weak, the diffusion current remains strong, allowing majority carriers to intuitively travel down their concentration gradient [8].

After charge carriers travel from the heterojunction to the anode and cathode, they can be extracted from the electrodes. This process reaches an optimized efficiency when the work done by the anode equals the HOMO donor energy and the work done by the cathode equals the LUMO acceptor energy. To obtain characteristics, elements are chosen that match these energies. For example, anodes are typically made of gold or indium tin oxide, matching the level of the HOMO donor P3HT used in this project. Similarly, cathodes are often made of aluminum, matching the level of the LUMO acceptor PCBM in this project [16].

Following collection, extraction occurs through the ohmic contacts that lie in between the active layer and the electrodes of the device.

## 2.3 Device performance metrics

Solar cell performance can be described through various parameters. The following highlighted quantities describe parameters most commonly used to characterize the performance of solar cells.

### 2.3.1 IV characteristics

*IV* curves are the most common method of characterization of solar cells. In dark conditions, the cell should appear as an ideal diode described by the Shockley equation [34]. Under illumination, however, the reverse current through the cell shifts the curve down. This

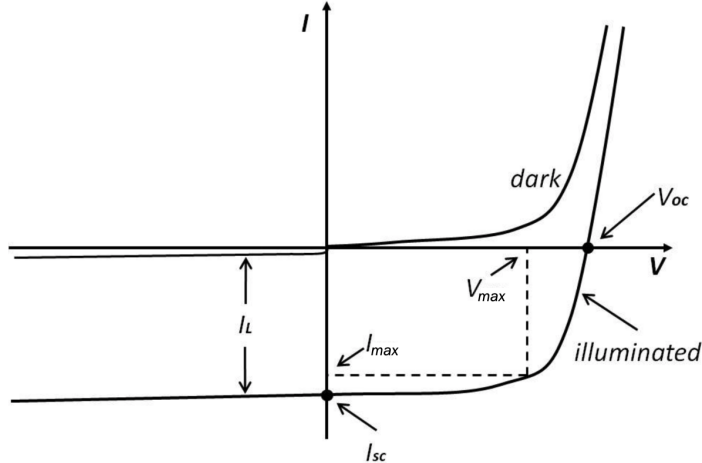


Figure 2.6: *IV* curve for a solar cell under dark and illuminated conditions.  $V_{OC}$  represent the maximum voltage that can be obtained from a solar cell when there is no current flowing through while  $I_{SC}$  represents the largest amount of current that can be extracted, and the current flowing through the cell when the voltage across it is zero.  $I_{mp}$  and  $V_{mp}$  are the current and voltage the cell should be operated at to attain its maximum power output. From [7].

project often implements the utility of *IV* curves to characterize global cell performance before implementing other imagine techniques. Outside of this investigation, *JV* curves are commonly used, implementing current density  $J$  (amps per square meter) as opposed to current  $I$  (amps) which allowed for device comparison of varying surface areas.

### 2.3.2 Open circuit voltage and short circuit current

A working solar cell can be understood through the characteristics that allow for power extraction, current and voltage. To yield an understanding of these quantities a working cell can be fixed with a load resistance. By Ohm's Law  $R_L = V/I$  which provides definitions for short and open circuit operations. For short-circuit operations, the load resistance should equal zero, while open-circuit measurements will yield an infinitely high load resistance [32]. At these points of measurement, we can also define a short-circuit current ( $I_{SC}$ ) and open-circuit voltage ( $V_{OC}$ ) where power will equal zero. These quantities are represented graphically in Fig. 2.6.

The open-circuit voltage represents the maximum voltage that a solar cell can produce. It is measured with an external load across the output terminals at zero net current.  $V_{OC}$  characterizes the upper limit of the LUMO acceptor and HOMO donor energy gap [32]. Similarly, at  $V_{OC}$  the diffusion and drift currents cancel each other out.

The short-circuit current similarly represents the maximum current production of a solar cell. It is measured without an external load with zero voltage across the terminals. In an ideal solar cell,  $I_{SC}$  equals the photogenerated current,  $I_L$  which is proportional to the intensity of incident light.

### 2.3.3 Fill factor

Power can be calculated on any point of an  $IV$  curve by using the relation  $P = IV$ . By inverting the current axis on the solar cell, the  $IV$  plot moves the curve into the first quadrant, where the area of the rectangle under the curve corresponds to power output, which can be seen in Fig. 2.7. The fill factor of a solar cell describes the ratio of the products of the current and the voltage that maximize power output to the product of  $V_{OC}$  and  $I_{SC}$  such that [34]

$$FF = \frac{V_{max}I_{max}}{V_{OC}I_{SC}} \quad (2.2)$$

Where the numerator is the area of the largest rectangle that can fit under the inverted curve, as shown in Fig. 2.7, where the fill factor is represented by the ratio of the area of the blue rectangle to the grey rectangle.

### 2.3.4 Power conversion efficiency

Efficiency is one of the most useful parameters in characterizing solar cell performance. Under control operating conditions of illumination by the air mass 1.5 solar spectrum (AM 1.5) and at an operating temperature of 298 K we can define  $\eta$  as

$$\eta = \frac{P_{out}}{P_{in}} = \frac{V_{oc}I_{sc}FF}{P_{in}}, \quad (2.3)$$

or the fraction of power input  $P_{in}$  from incident photons that are outputted to electrical power.

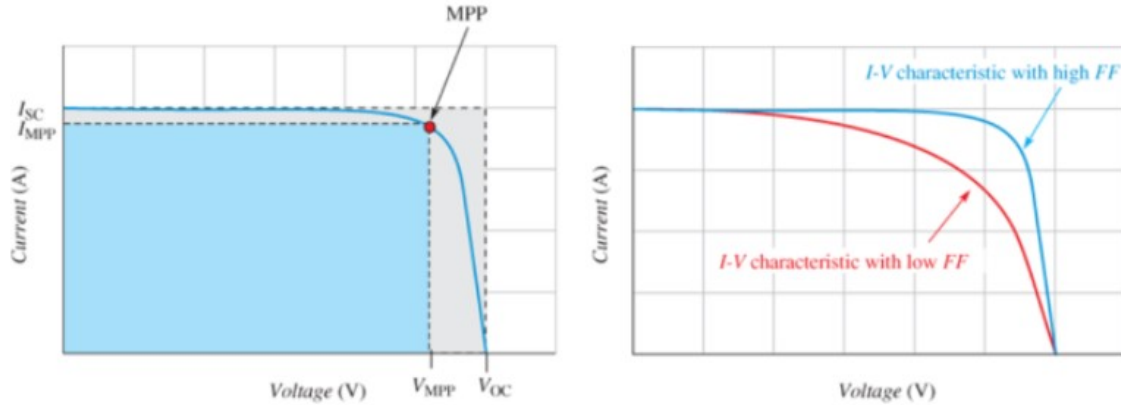


Figure 2.7: Graphical representation of the fill factor for a solar cell. *IV* curve "squareness" relating actual output to the theoretical (left). Two *IV* curves demonstrating high and low fill factors. From [7].

This chapter outlined the structure and mechanisms for operating inorganic and organic solar cells. Their differences were outlined, followed by a discussion of significant metrics that characterize performance.

# Chapter 3

## Methods

The following chapter describes the experimental methodologies relevant to the project. First, the development of the in-house devices is discussed, followed by the experimental set ups for extracting various data from the cell. The chapter ends with a discussion of various imaging techniques used in the literature, and finally the procedure and algorithm used in this research.

### 3.1 Experimental Devices

#### 3.1.1 P3HT:PCBM cells

The experimental devices used in this thesis were fabricated in Professor Tanenbaum's lab using the method developed by Sabrina Li PO'17. Each device consists of six cells named for their active layer containing poly(3-hexylthiophene 2,5-diyl) (P3HT), and phenyl-C<sub>61</sub>-butyric-acid-methyl ester (PCBM). The P3HT PCBM devices exhibit an inverted geometry in which light shines on the cell through the bottom glass substrate and semi-transparent ITO layers, whereas the contacts are accessed from the top.

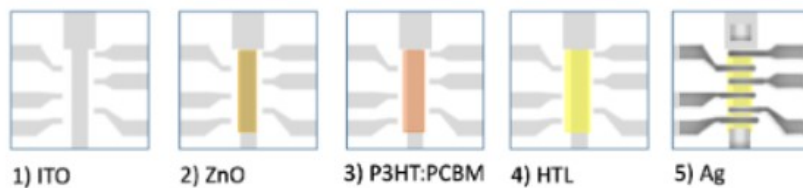


Figure 3.1: Layering of applied materials of P3HT:PCBM cells [9]

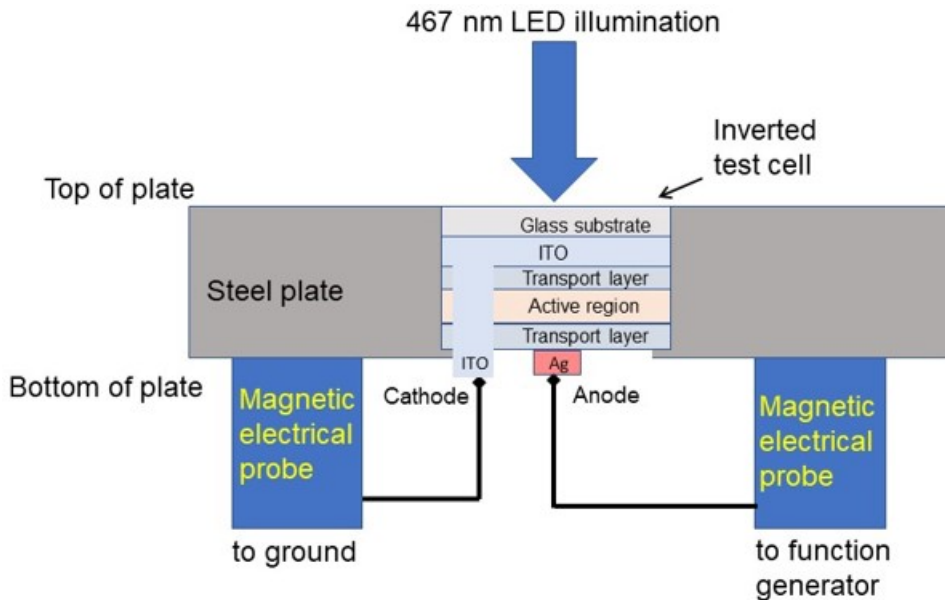


Figure 3.2: Cross section of P3HT:PCBM in-house cells.

### Device manufacture and layout

Each chip contains six  $3mm^2$  sized cells that branch out from the central vertical strip of the semi-transparent metallic ITO, which serves as the cathode. The top silver layer (Ag) overlays the central strip to allow for the active contacts seen in Fig. 3.1.

Fig. 3.1 displays the fabrication layers for the P3HT:PCBM cells while Figure 3.2 shows a cross section of the cells as they are connected in the lab set up. The cells exhibit an inverted geometry that differs from conventional geometries in that the layering of the anode and cathode, hole and electron transport layers are reversed. In conventional geometries, the anode is transparent which allows for the absorption in the active region through to the hole layer, Inverted geometries provide that the cathode is transparent, with absorption through the active region to the electron transport layer.

The materials that comprise the cells are equally important in providing for its efficiency. In layering order, indium tin oxide (ITO) is laid on the glass substrate and serves as the cathode, zinc oxide ( $ZnO$ ) provides the electron transport layer, P3HT donates electrons while PCBM accepts, various materials can be applied for the hole transport later (HTL),and silver (Ag) is the anode. Different to conventional cells, photons enter through the ITO and migrate through the hole transport layer to the anode, Ag.

## 3.2 Chip mount

In order to perform characterization methods on the cells, a novel setup was created. The previous setup featured a clear plastic pane fixed over top of the chip by adjusting a pair of

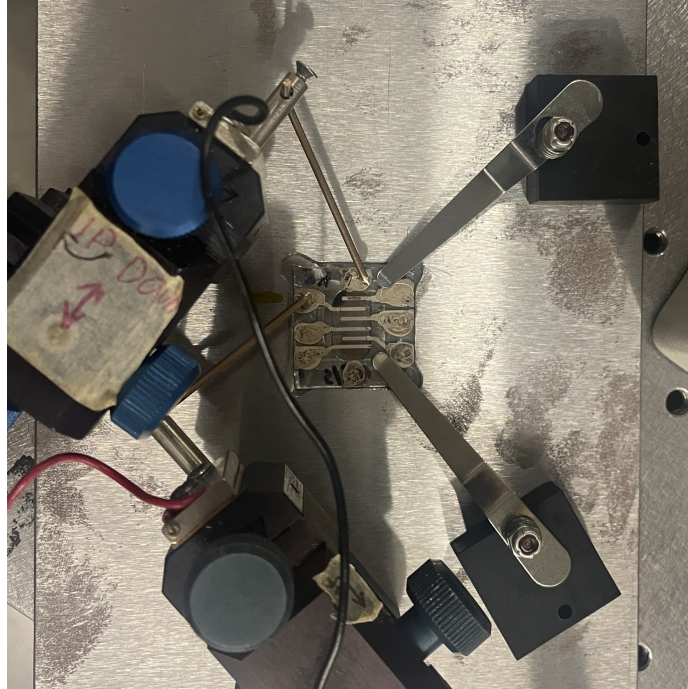


Figure 3.3: Mobile magnetic plate setup. The cell is probed at the contacts to be characterized either by IV curves or Thermoreflectance imaging.

screws on either side of the pane. The device was aligned with seven spring-loaded, rounded metal pins that served as electrical contacts that lined up with the specific architecture [16]. However, the pressure from screwing the top on to secure the contacts was cracking the chip, thus eliciting a new design to preserve the chip conditions. The setup is based on a steel plate with a laser-cut oblong hole at its center for sample exposure to light. The plate setup was constructed to be portable.

The plate features a recessed square underneath the oblong exposure to hold the device and provide space for contacts to supply a voltage and bias a given cell. The device sits within the recessed square and is held in by magnetic clamps that magnetically adhere to the plate. Similarly, probes on mobile magnetic mounts can be adhered to the plate to provide contacts for characterization. This setup provides cell protection and precision that the previous setup did not offer. The setup was developed with Hardy Richardson.

### 3.3 *IV* curve setup

Current over voltage or *IV* curves provide the initial method of OPV characterization. The plate setup was used with the recessed side exposed, allowing for ease of measurement among cells on the chip. The chip enables top contact to the cathode at two locations, as well as individually accessible anode contacts for each of the six cells. The magnetic probes and clamps were used to secure the device and supply the voltage bias. The voltage bias was

supplied by a Keithley SMU2400 source meter, which can be controlled through the Labview program developed by Taylor Venenciano PO'23.

### Sunbrick

The setup to measure the IV characteristics of the cells was greatly improved by the addition of the Sunbrick lamp seen in Fig. 3.4. The Sunbrick is an indoor solar simulator that uses LED illumination to test the responses of light-sensitive materials such as solar cells [36]. Using the novel mounting setup, the device can be placed under the Sunbrick when connected to the contacts for measurement. The contacts are connected to a Keithly SMU2400 source meter that sweeps the voltage applied to the cell over a user-determined range, while measuring the resulting current. The Sunbrick is connected to a digital program on a laptop

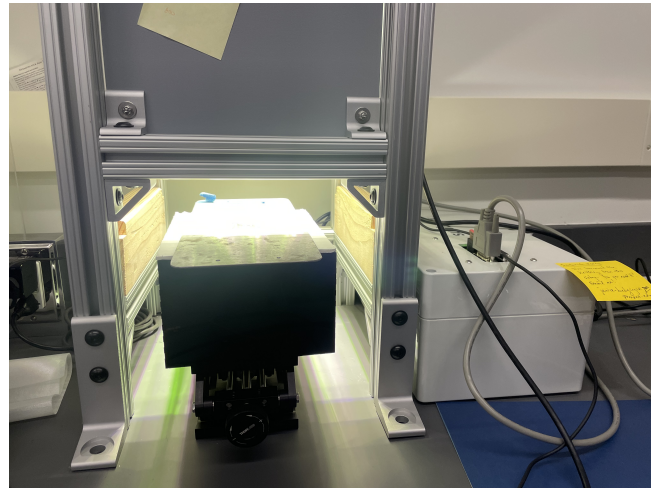


Figure 3.4: Sunbrick solar simulator with mobile magnetic mount under illumination.

that provides a given spectrum to supply the device with to simulate solar activity. For our measurements, the 'am1.5g-1.0' spectrum was used as it is equivalent to 1 sun [36]. After allowing the Sunbrick to load the spectrum for 30 minutes, measurements are taken.

### Labview program

Used in tandem with the Sunbrick, the Labview program, written by Taylor Venenciano '23, provides the IV characteristic of the measured cell. The program allows for modification of start/stop voltage, step size, etc, where the typical settings to determine cell performance at set at a start voltage of -0.2 V and a stop voltage of 1 V, step size of 0.01, a current limit of 1 A, averaging each data point over a number of measurements that can be controlled in the program, typically ranging from 1 to 100. The settings can be modulated based on the characteristics of the sample, however the standard settings were used in this investigation.

The *IV* characteristics were compared with those of a traditional diode to determine optimally performing cells that can then be further characterized by the Thermoreflectance

imaging system. Additionally, the curves are evaluated based on their response to light and thus their ability to perform photoelectric energy conversion. Under dark conditions, the curve should resemble an ideal diode equation curve. When illuminated by a light source, the entire curve is vertically translated down. In this case, current from the cell is taken to be negative because voltage at the cell terminals are positive while current exits the cells. Thus the cell sinks current, corresponding to the negative sign convention.

## 3.4 Imaging techniques

As solar cell research has developed, a suite of imaging techniques have characterized cell efficiencies and defects. While invasive imaging techniques such as atomic force microscopy and scanning electron microscopy allow for atomic-scale resolutions, they can also be destructive to cell performance. The following methods are not intrusive, with this project implementing a non-invasive thermography technique.

### 3.4.1 Fluorescence microscopy

Fluorescence microscopy developed as a technique to spatially relate material properties of devices to optical properties. It is often implemented to image small-scale features to visually enhance their presence. This is possible in devices that contain compounds that fluoresce as they degrade during the imaging process. The image then captures this radiation of the degradation of the compounds [37].

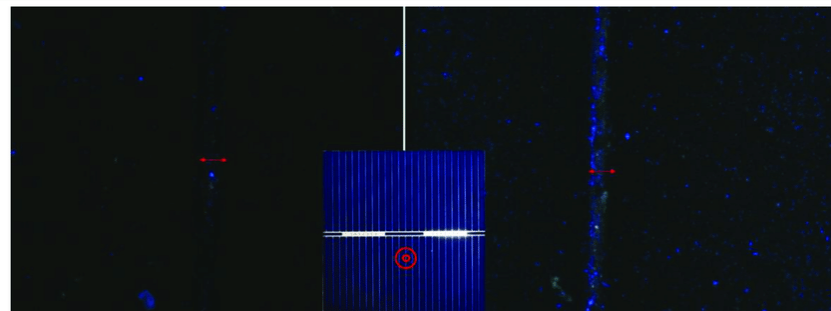


Figure 3.5: Fluorescence microscopy of two poly-Si solar cells. Bare cell (left), bare p-c-Si solar cell with concentric circles indicating a region of  $\times 10$  higher microscopy (middle), Coated sample with PA Si-QDs (right). The arrows indicate the position of a silver finger. From [10]

### Luminescence imaging

Luminescence imaging is a similar form of microscopy that excites the active layer of a sample device to generate excitons or luminesce. A camera is used to capture an image of the subsequent exciton decay and radiation of light [38].

Electroluminescence (EL) imaging involves the application of a constant current or voltage to a sample device through electrical contacts and thus only images solar cells post-production. The current or voltage applied generates a recombination of charge carriers in the active layer that is detected by the camera to image the cell [38].

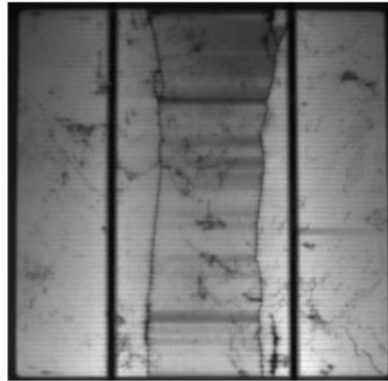


Figure 3.6: An EL image of a multicrystalline solar module exhibiting two large cracks. From [11]

Photoluminescence (PL) imaging optically excites the sample which allows for broader application than EL imaging. Similarly, PL imaging implements a non-contact technique which allows for mechanical preservation of the sample [12].

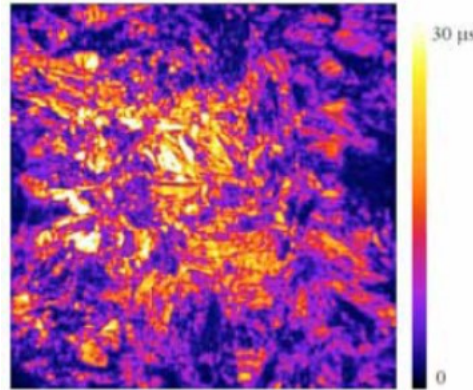


Figure 3.7: PL image of a six-inch SiN multicrystalline silicon wafer demonstrating effective minority carrier lifetime. Attained megapixel resolution in < 1 s. From [12]

### 3.4.2 Light beam induced current (LBIC)

LBIC involves light stimulation from a point laser to generate a map of short-circuit current or photocurrent in a sample device. The measurement period is quick and provides a high resolution image that presents a spatially resolved image of recombination active defects,

providing information as to degradation of cell performance manifests over time. However, LBIC is rarely done on larger scale thin-film solar modules because of continued issues with signal recovery [13].

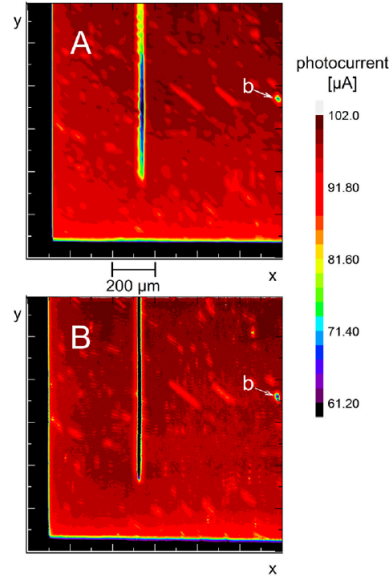


Figure 3.8: LBIC images of a thin-film CIGS solar cell. Dark red represents the maximum photocurrent of 102 micro amps. Map A was measured with 10 micro meter steps, while map B uses 4 micro meter steps. Map B presents a higher resolution, indicated by the 10 micro meter wide contact finger (vertical black line). [13]

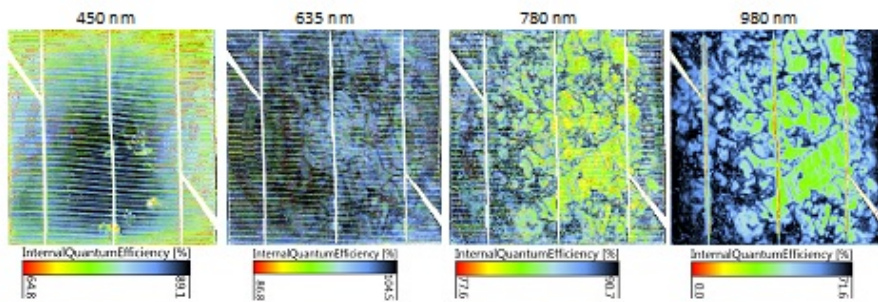


Figure 3.9: Internal quantum efficiency measurements of a solar cell at four different wavelengths. From [14]

### 3.4.3 Thermal imaging

This project focuses on non-invasive Thermoreflectance (TR) imaging, a form of a larger set of thermal imaging techniques. Invasive thermography techniques such as scanning thermal microscopy and liquid crystal thermography are able to measure the temperatures of micro and sub-micrometer devices, however their methods threaten to damage the device and their functionality after imaging [15]. Non-invasive thermography techniques such as dark lock-in thermography or infrared (IR) thermography allow for spatial temperature mapping without the threat of device degradation, however background radiation and noise limit their use.

This project implements the use of TR imaging. TR imaging is an advantageous technique that provides higher resolutions than other thermography techniques (250 nm as opposed to 10-20mK for IR) and is adept at characterizing local shunts and other defects in solar cells. Performing quantitative analyses such as localized *IV* curves and field performance metrics on the spatially resolved map provides more information on the physical origins of these defects.

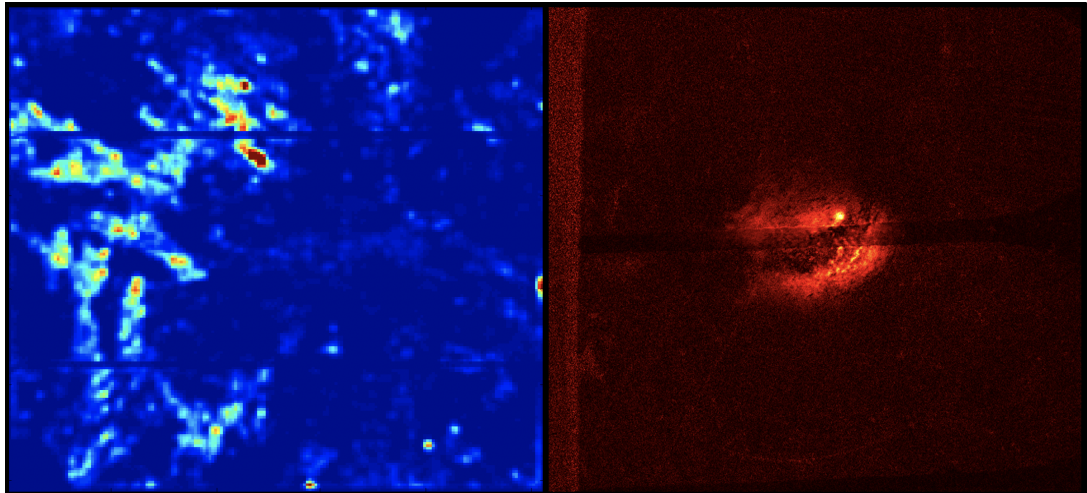


Figure 3.10: Dark lock-in thermography image of a silicon solar cell. Breakdowns are indicated by the red regions of higher temperature (left) From [15]. TR image of a 9x9mm region of an organic solar cell. Brighter coloring indicates greater relative heating to the rest of the cell. (right)

## 3.5 Thermoreflectance imaging system

The TR imaging system measures a change in surface reflectivity  $\Delta R$  as a response to temperature modulation  $\Delta T$  induced by a current or voltage. This relationship  $\Delta R/R$  is provided by

$$\frac{\Delta R}{R} = \frac{1}{R} \frac{dR}{dT} \Delta T = \kappa \Delta T, \quad (3.1)$$

where  $R$  is the surface reflectivity,  $T$  is the temperature modulation, and  $\kappa$  is the thermoreflectance coefficient.  $\kappa$  is a calibration constant that is determined by the material being tested.

The same mounting setup for IV curves is used for the Thermoreflectance imaging system. However, the plate is flipped with the oblong cut side up to expose it for photostimulation through the objective provided by a 467nm blue light LED.

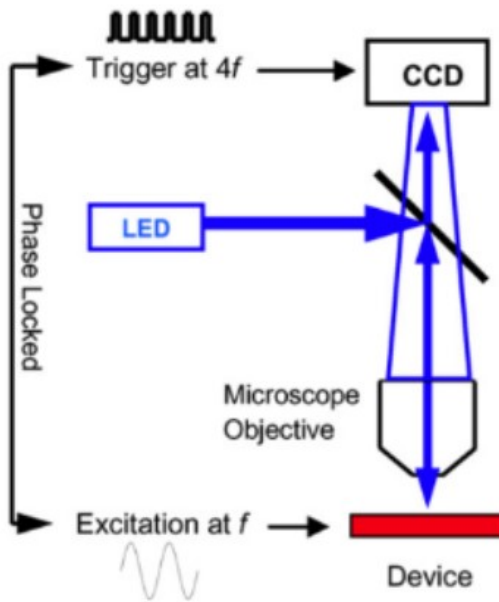


Figure 3.11: Schematic of the thermoreflectance imaging system. From [16]

To provide the thermal modulation required to image, the sample is excited ( $\Delta T$ ) using a sinusoidal voltage modulation at a fixed frequency of  $f_s = 10\text{Hz}$ . The sample is stimulated by the blue LED that is DC biased between 5 and 20 mA by an ILX Lightwave Precision Laser Diode Current Source and imaged by an Opteon Si CCD camera attached to a Nikon Optishot standard light microscope. Electrical bias is applied to the sample through a Tektronix AFG 3022B Dual Channel Arbitrary Function Generator. The function generator both sinusoidally modulates the voltage into an ILX Lightwave LDX3220 Precision Laser Diode Current Source at  $f_s$  and sends square TTL pulses. The square pulses are phased-locked to the modulation of the sample of 5V amplitude to the camera at  $f_c = 4f_s = 40\text{Hz}$ , triggering the opening and closing of the shutters for imaging. The imaging setup is shown in Fig. 3.3 and Fig. 3.11.

### 3.5.1 Amplitude and Phase maps

Using the imaging setup, an algorithm that implements a four-point discrete Fourier Transform Technique calculates the amplitude and phase at each pixel of the generated images [16]. The reflectance of the sample surface at each pixel, denoted by coordinates  $(x, y)$ , at time  $t$  can be understood through the following relation

$$R_{x,y}(t) = c(x, y) + \Delta(x, y) \cos(2\pi f_s t) + \phi(x, y) + \Phi \quad (3.2)$$

where the DC component  $c(x, y)$  describes the DC background reflection, and the AC component  $\Delta(x, y)$  describes the modulated sample reflection. The phase  $\phi(x, y)$  is proportional to the time taken for heat to spread within the sample, and the arbitrary phase  $\Phi$  accounts for the time delay modulation in the electronics. As the camera images at a rate

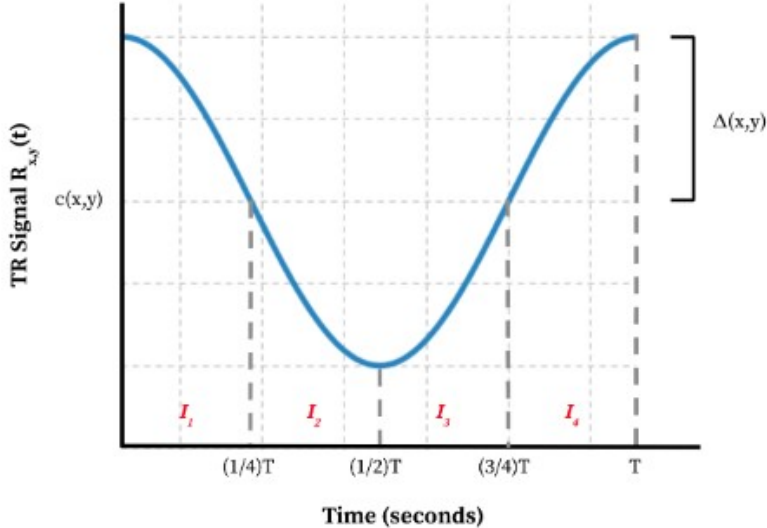


Figure 3.12: Plot of Thermoreflectance signal over one and a quarter modulation periods. From [16]

four times that of the sample excitation frequency  $f_s$ , photons are collected by the camera in each of the four quarters of the sample modulation period  $T$ . In each quarter period the camera effectively integrates over the thermoreflectance signal  $R_{x,y}(t)$  and divides by  $T/4$ . These values are subsequently stored in four image buffers or 'buckets,' visually understood through Fig. 3.12. A single modulation period of the sample yields four buckets,  $I_1$ ,  $I_2$ ,  $I_3$ , and  $I_4$ , which can be modeled in the case of no noise as:

$$I_k = \int_{(k-1)T/4}^{kT/4} c + \Delta \sin(\omega t + \phi) dt, \quad k \in \{1, 2, 3, 4\}. \quad (3.3)$$

Where the total buckets are summed over N modulation cycles of the average reflectance within the  $k$ th quarter period. The N required for image generation in this investigation ranges between 20,000 and 200,000 iterations so as to reduce inherent noise in the data acquisition process.

After the data acquisition period, the amplitude and phase can be calculated at each pixel point using the following equations. The relative amplitude of the signal is:

$$\frac{\Delta R}{R} = \frac{\pi}{\sqrt{2}} \frac{\sqrt{(I_1 - I_3)^2 + (I_2 - I_4)^2}}{I_1 + I_2 + I_3 + I_4}. \quad (3.4)$$

Likewise, the phase  $\phi$  is calculated using:

$$\phi = \arctan \frac{(I_1 - I_3) - (I_2 - I_4)}{(I_1 - I_3) + (I_2 - I_4)} \quad (3.5)$$

In a typical measurement, the camera images during each quarter period are summed into their respective buckets,  $I_1$  to  $I_4$  over 10,000 to 20,000 sample modulation periods. MATLAB is then used to calculate  $\Delta R/R$  and  $\phi$  at each pixel to generate an image, such as Fig. 3.13.

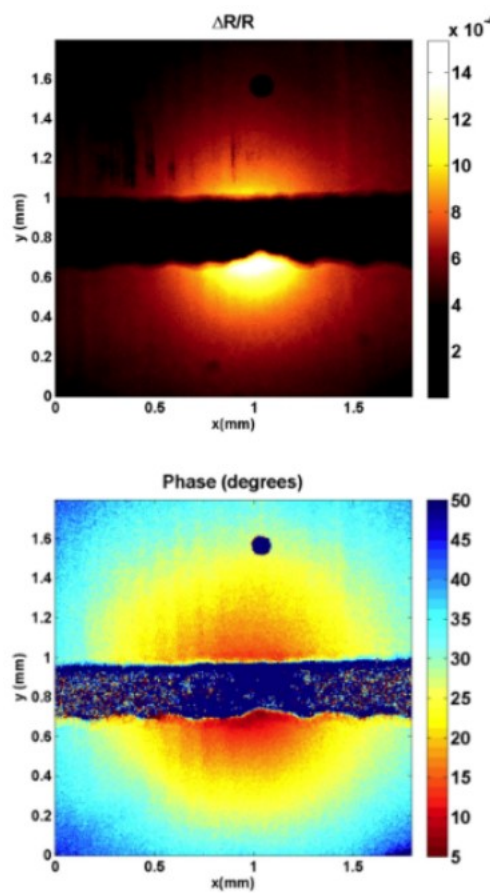


Figure 3.13: From  $\Delta R/R$  and  $\phi$  images of a commercial Evergreen silicon solar cell. From [17]

# Chapter 4

## Characterizing defects

This chapter first outlines the mechanisms responsible for a variety of defects in solar cells, following up with a discussion of categories of defects outlined in the literature and their signatures in various imaging techniques discussed in the previous chapter. The chapter finishes with a discussion of passivation methods of defects to improve cell performance.

### 4.1 Defect origins

Defects manifest in a multitude of ways, leading potential alterations to the basic structural components of the cell and optoelectronic component, thus affecting the performance of the device.

Fig. 4.1 details the alterations to the physical structure of the cell from defects. Defects vary by magnitude of disruption in the structure from point defects altering individual ion locations, to paired defects that alter the efficiency of photo absorption mechanisms, to higher dimensional defects that alter multiple performance mechanisms. Often smaller scale point defects can influence cell performance enough to become larger dimensional defects [18].

#### 4.1.1 Crystallization

Earlier generations of solar cells such as mono and polycrystalline (or multicrystalline) silicon are produced through various crystal production mechanisms to form their structure. In recent years, these types of solar cells have begun to introduce other elements in their synthesis to avoid the price and chemical synthesis of pure silicon, as well as potentially increase the efficiency of solar devices. The introduction of other elements into the silicon ingot - the manufacturing stage between polysilicon and the wafer - has been responsible for the altering of crystal structures in solar devices [39]. The cells often exhibit imperfect lattice structures as well as the introduction of other atoms from the novel elements or from the environment have been responsible for defects within the crystal structure of solar cells.

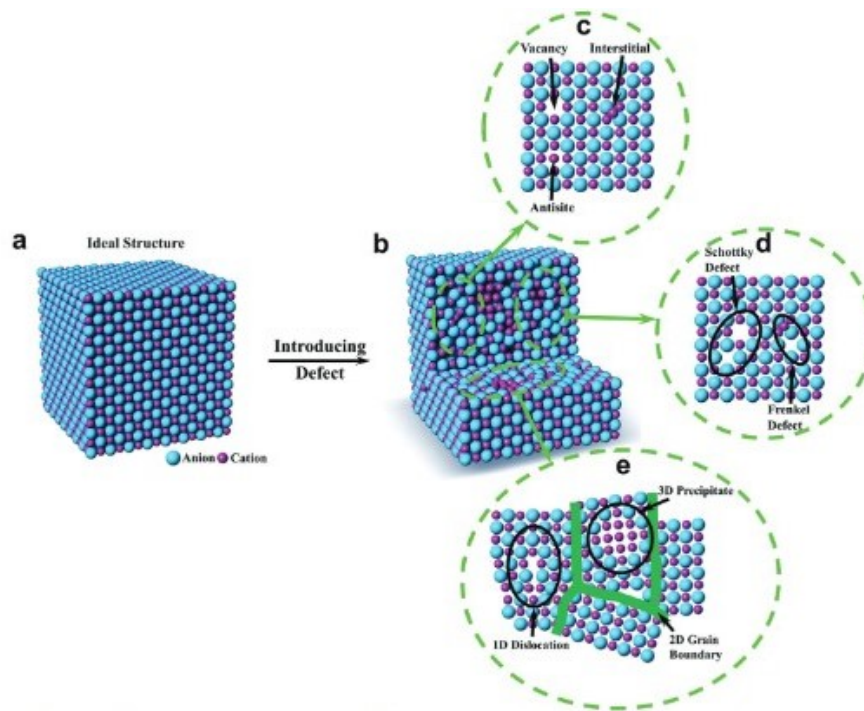


Figure 4.1: Introduction of defects in the crystal structure of a solar cell.(a) Ideal crystal structure without defects; (b) after defect introduction; (c) point defects;(d) paired defects; and (e) widespread defects. Adapted from [18]

### 4.1.2 Fabrication mechanisms

One of the many challenges facing solar cell mass production is the reproducability of device production conditions, performance, and characteristics. Many defects can arise during the production process as unevenly deposited emitters, contacts, and device layers.

The fabrication of components contains variability in each step. As mentioned in the previous section, chemical impurities introduction in ingot manufacturing can cause element precipitation into the device and alter bonds that affect charge carrier recombination and other processes during photoelectric conversion. When heating silicon before crystallization in the crucible - a cup-shaped piece of laboratory equipment typically made of porcelain or an inert metal used to contain chemical compounds when heating them to high temperatures - impurities from the ambient can also be introduced to generate similar defects [19]. Alternatively, gas phase formations can be used in chemical synthesis of cells to lower production costs, however diffuse emitters and chemical intrusion defects are possible[40]. The development of coating processes such as spin, spray, blade, or push coating have improved defect passivation mechanisms, however chemical impurities are still present.

Finally, solar devices are susceptible to their environment. Prolonged exposure to moisture in the air and extreme temperatures can induce thermal or mechanical stresses on the optoelectronic components of the devices such as inducing a lower breakdown voltage or

trapping charges in grain boundaries [8]. While OPVs do not experience defects during crystallization processes, their organic nature makes them significantly more susceptible to ambient conditions, often leading to degradation over time.

## 4.2 Defect types

Defects in solar cells can manifest in a number of different ways, with their characteristics and mechanisms often specific to cell type and production. Broadly, we can categorize two types of widespread defects as either inducing a trapped state or a shunt, some defect producing both. The subsequent categories describe the point and paired defects that influence the existence of widespread defects. Trapped states and shunts affect cell performance in at varying stages of the photoelectric energy conversion process and are induced by different mechanisms. We can then categorize how defects induce trapped states or shunts, and how those manifest in characterization methods.

### 4.2.1 Shunts

Shunts are inadvertent current paths created that exhibit less resistance than passing through the load [38]. Thus, the current will use the shunt to bypass the main path that exhibits typically greater resistance through the circuit. Since the current will not pass through the load, the overall current and voltage across the device will decrease. Ideally, the shunt resistance,  $R_{sh}$ , goes to infinity, diverting zero current from the load. Following this, the series resistance,  $R_s$ , goes to zero, encouraging current through the load.

### 4.2.2 Trap states

The other broad category of defects are known as trap states. Trap states are energy levels that lie between the HOMO/LUMO band gaps that cause charge carriers to be trapped inside a material, leading to device deficiencies. The defects insert an energy transition level into the band gap of a semiconductor that specially traps free charges and change charge recombination pathways [41]. The mechanisms of charge recombination are illustrated in Fig. 4.2.

Trap states are largely determined by the location of their energy levels relative to conduction band minimum (CBM) or valence band maximum (VBM) edge. The CBM represents the lowest energy level in the conduction band, while the VBM is the highest energy level in the valence band [41]. The CBM and VBM are determined by the structure of the material used in the device, and can be tuned by changing its chemical composition. Traps also exhibit either shallow level or deep level qualities as demonstrated in Fig. 4.3. Traps are "deep" in the sense that the energy required to move a charge carrier from the trap to the valence or conduction band is much larger than the characteristic thermal energy [41]. Shallow level trap states are localized states that induce shallower transition energy levels.

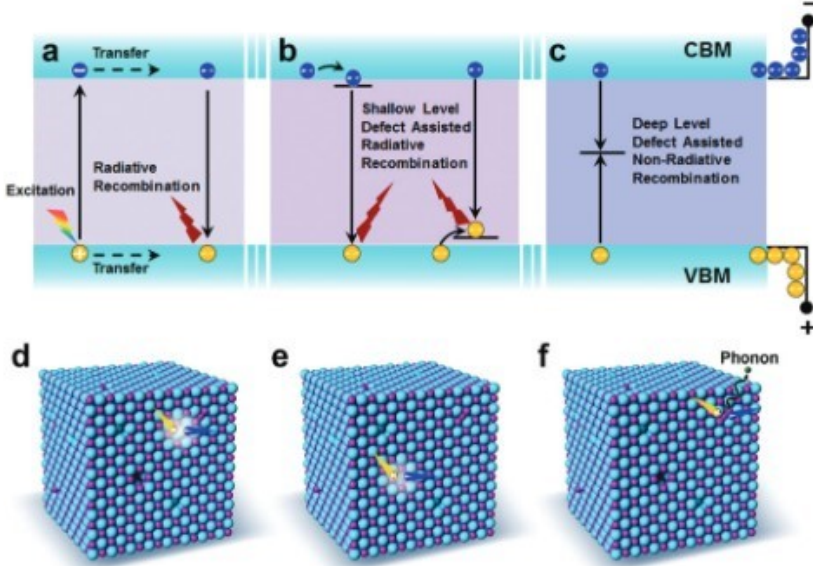


Figure 4.2: Potential charge recombination pathways in semiconductors. (a) "Band-to-Band," a radiative process involving transition of excited electrons at the CBM back to the ground state to recombine with holes at the VBM, (b) Shallow-level trap, (c) Deep-level trap exhibiting non-radiative recombination, (d) "Band-to-Band" recombination where no defects are present, (e) Shallow-level defect radiative recombination, and (f) Deep-level defect non-radiative recombination. Adapted from [18]

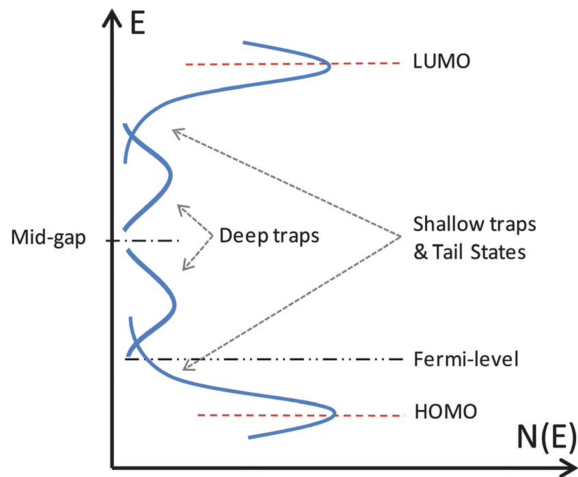


Figure 4.3: Conceptual illustration of the density of states in an OPV. From [7]

Ideally, photo excitation encourages electrons from ground at VBM to become excited states at CBM and subsequently free charges. However, shallow level traps create energy

transition levels in the band gap close to the CBM or VBM of the material structure so that trapped charges have to choice to either recombine or detrap back of the CBM or VBM through photon absorption [41]. This process results in an energy loss that encourages further charge recombination and even has the potential to enhance device properties. Deep level traps require charges to annihilate the opposite charge before emission. This process described non-radiative recombination, where shallow level traps exhibited radioactive recombination. Non-radiative recombination, however dramatically decreases the capability of optoelectronic properties and are much more of a threat to cell performance [18].

Traps can be characterized as intrinsic or extrinsic. Extrinsic traps are inhabited when chemical modifications to the cell occur such as exposure to impurities during material synthesis or device fabrication, exposure to oxygen, etc. Intrinsic traps are induced from imperfections in the amorphous nature of thin films. They are morphological alterations that modify the energetic components of the cell and generate states shallower than the band gap [18]. Traps are harmful because they can alter the optoelectronic properties of the cells and introduce recombination centers, yielding losses in the short circuit current density,  $J_{SC}$ , open circuit voltage,  $V_{OC}$ , and fill factor,  $FF$ , lowering the overall photoelectric conversion efficiency,  $\eta$ .

### 4.2.3 Chemical impurities

For older generations of silicon solar cells, chemical defects typically manifest as point or paired defects through complications in the crystallization process and intrusions of introduced elements for easier synthesis. In more recent developments of silicon cells and emergent technologies, exposure to ambient elements are responsible.

#### Iron

Iron is the most prominent elemental intrusion in crystalline solar cells. Most equipment and devices to facilitate the growth of ingots prior to wafer processing consist of an iron base, often introduced in silicon feedstocks or crucibles. Iron has also been introduced to passivate other types of defects. Iron intrusions can facilitate defects in the crystal structure and at grain boundaries, altering recombination pathways and decreasing the diffusion length for charge carriers [39].

#### Oxygen

Oxygen is another common element responsible for defects in solar cells. In earlier device generations it is most commonly found interstitially, or in between device layers. In emergent technologies, atmospheric oxygen may induce doping of the active layer that leads to deep traps [42]. Interstitial oxygen is often the result of the partial dissolution of crucible walls or coating, as well as interactions with molten silicon in the fabrication process [19]. The harm of interstitial oxygen is found in their ability to form boron complexes and become thermal donors. Boron complexes occur when silicon is doped with boron due to their similar binding

structures. These chemical formations can trap and reduce minority carrier lifetime and subsequently cell efficiency. Interstitial oxygen can also form thermal donors, typically between 300 and 500 degrees Celsius in Czochralski silicon cell types. Thermal donors are electrically active oxygen complexes consisting of small groupings of oxygen atoms that elicit unpredictable effects on device performance; either producing charge recombination sites from dangling bonds between the silicon interface and themselves or potentially improving crystal formation [42]. In OPVs, oxygen-induced doping of the active layer invites trapping mechanisms to alter charge recombination mechanisms, but is still largely understudied.

## Nitrogen

Nitrogen impurities are common in multicrystalline solar cells that experience other types of crystal defects such as grain boundaries and dislocations. Nitrogen is often introduced to silicon ingots to prevent cracking in the coating process, however their bonding structures weaken during solidification due to weaker convection of molten silicon, so the element can permeate through and create dislocations. Inactive and thermal donor forms are most commonly encountered but present minimal harm to device performance. Si<sub>3</sub>N<sub>4</sub> is found in rods, fibers, and nets presenting high resistivity and mechanical stress on the device due to mismatches in the crystal lattice, eliciting dislocations [20]. Fig. 4.4 demonstrates the appearance and characteristics of nitrogen inclusions under IR microscopy.

## Carbon

Carbon impurities most commonly occur as point defects substituting atoms due to atmospheric exposure leading to vapor absorption. If the amount carbon atoms exceeds a given solubility limit, it can form precipitates that induce ohmic shunts. Fig. 4.4 showcases the particle and filament forms of carbon under IR microscopy, highlighting their ability to alter the crystalline structure of monocrystalline cells. Other elements have been known to produce defects such as copper. Similar to iron, copper introduces recombination centers that decrease minority carrier lifetime [20]. The chemistry related to other elemental defects lies outside the scope of this project.

### 4.2.4 Structural alterations

Structural defects can alter the composition of the cell at a point level to widespread defects. In older device generations, crystal defects dominate, originating during variable growth conditions and subsequently reducing carrier diffusion lengths. Emergent technologies, especially OPVs benefit from synthesis and substrates that limit structural defects, however perovskites still experience alterations to the crystalline structure.

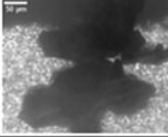
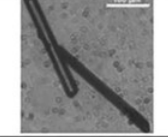
type	SiC particles	SiC filaments	Si <sub>3</sub> N <sub>4</sub> rods	Si <sub>3</sub> N <sub>4</sub> fibers	Si <sub>3</sub> N <sub>4</sub> nets
IR microscopy					
size	1–600 µm in diameter	<5 µm in diameter, up to 3 mm in length	<30 µm in diameter, up to 2 mm in length	<500 nm in diameter, up to 8 mm in length	<500 nm in diameter, up to 3 mm in length
morphology	compact particles, frequently in clusters showing irregular surface and consisting of monocrystalline particles showing vicinal faces	irregular diameter, rough surface, multicrystalline	polygonal diameter, smooth surface, monocrystalline	steady diameter, smooth surface, monocrystalline	irregular diameter, smooth surface, multicrystalline
local growth preference	within grain volume, often at Si <sub>3</sub> N <sub>4</sub> rods	mostly in grain boundaries, growing in crystallization direction	within grain volume, random orientation	within grain volume, growing in crystallization direction, branching	in grain boundaries, growing in crystallization direction
crystal structure	cubic, β-SiC	cubic, β-SiC	hexagonal, β-Si <sub>3</sub> N <sub>4</sub>	trigonal, α-Si <sub>3</sub> N <sub>4</sub>	trigonal, α-Si <sub>3</sub> N <sub>4</sub>
space group	F43m (216)	F43m (216)	P63 (173)	P31c (159)	P31c (159)
lattice constants	$a = 0.436 \text{ nm}$	$a = 0.436 \text{ nm}$	$a = 0.760 \text{ nm}$ , $c = 0.291 \text{ nm}$	$a = 0.775 \text{ nm}$ , $c = 0.562 \text{ nm}$	$a = 0.775 \text{ nm}$ , $c = 0.562 \text{ nm}$
impurities	N, Al	N, O	Li, C, O, Mg, Ca	C, O, Ca	C, O, Al, Ca
electrical resistance	$8.17 \times 10^{-5} \Omega \text{ cm}$ (4PP)	$2 \times 10^{-3} \Omega \text{ cm}$ (4PP) [28]	$>4.7 \times 10^7 \Omega \text{ cm}$ (4PP) [28]	$(5 \pm 4) \times 10^8 \Omega \text{ cm}$ (2PP)	$(1.44 \pm 0.26) \times 10^{10} \Omega \text{ cm}$ (2PP)

Figure 4.4: Classifications of chemical intrusions in monocrystalline silicon cells. From [19]

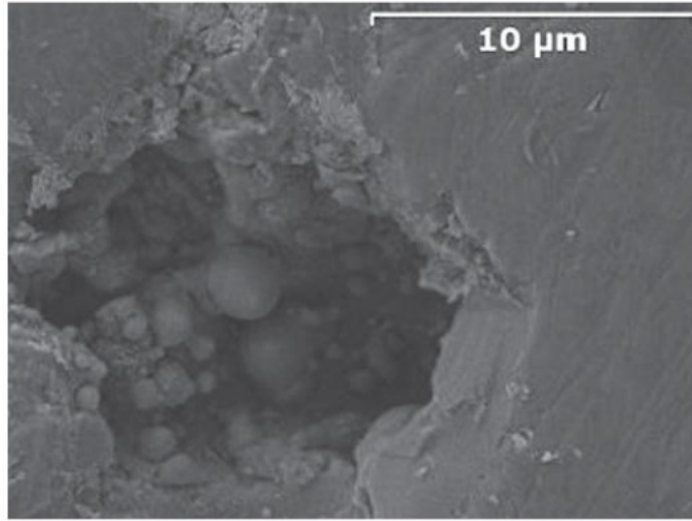


Figure 4.5: A SEM image of a dark grain boundary. Carbon and oxygen precipitates and voids can be observed. From [20]

## Grain boundaries

Grain boundaries (GBs) are the interfaces between two grains or crystallites in a polycrystalline material [43]. Their existence does not elicit defects on their own however, they often become sites of charge recombination, crystal formation, and elemental precipitates from their topographic features, seen in Fig. 4.5. The boundaries can exhibit many qualities from dislocations, twins, and the generation of subgrain boundaries as a result of incomplete or broken bonds or the misalignment of the crystal structures. These qualities can become enhanced in the presence of chemical impurities, inducing mechanical stresses and recombination sites that cause the device to inhabit trap states. In such cases, charge carriers become trapped in the GB with an energy level within the band gap, causing them to recombine with the opposing charge carrier instead of being extracted or separated, further depleting device metrics such as  $V_{OC}$  [43].

## Other crystal defects

Crystal defects off of the boundary include point defects such as vacancies or interstitial atoms, dislocations, stacking faults, and clusters. Vacancies are localized atoms missing from their regular positions in the lattice. Similarly, interstitials are impurity atoms that occupy the interstitial sites in the crystal lattice of the semiconductor [20]. The effects of specific interstitial atoms are described in the previous section. Dislocations are often the result of impurities or thermal or mechanical stresses in the crystal lattice. Stacking faults typically arise during crystal growth and are the result of errors that occur in the sequence of repeating patterns of layers of atoms. Clusters are the agglomeration of crystal defects in formations that magnify their degradation mechanisms, lowering performance metrics such as  $V_{OC}$  and  $I_{SC}$  [44]. The advantageous nature of the substrates of OPVs do not elicit crystal defects, however other emergent technologies such as perovskites can be subject to their effects.

Fig. 4.6 shows an LBIC scan displaying internal quantum efficiency (IQE) measurements of a Ribbon Growth on Substrate (RGS) silicon wafer. This type of silicon cells are casted directly from the silicon melt onto reusable substrates making them of the multicrystalline form [20]. This imaging approach is useful in identifying defects as the microscopy image detects the physical crystal defect components, GB clusters highlighted in the white rectangle, and shunt clusters highlighted in the black rectangle. In combination with the IQE measurements, it can be understood that the GB clusters exhibit a lower IQE as opposed to the higher shunt defects, yielding information on improving efficiencies at GBs.

Fig. 4.7 highlights defect clusters in a polycrystalline cell and chronicles their growth within the silicon ingot. Their location within the device suggest that they are GB and dislocation clusters. The EL image was taken at a very low luminescence intensity due to charge recombination losses from the defects. This imaging technique is useful as it traces the defect origins within cell development.

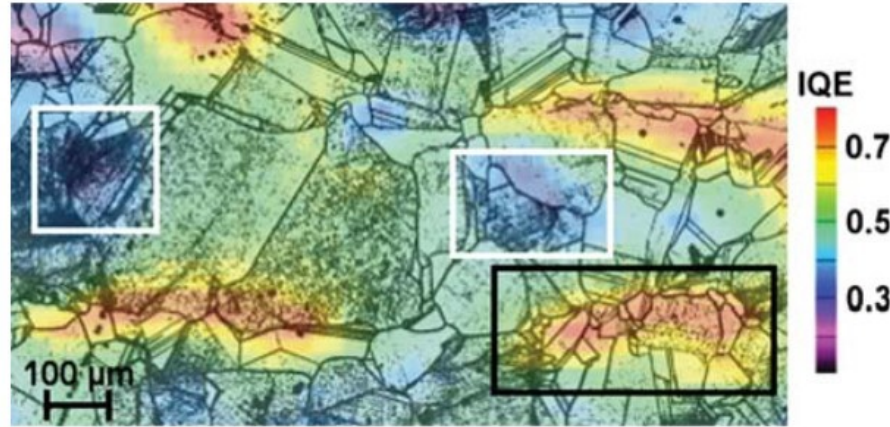


Figure 4.6: LBIC scan of an RGS silicon wafer over an optical microscopy image. Defective regions are highlighted in white rectangles, the black rectangle signifying a patterned region of current collection. From [20]

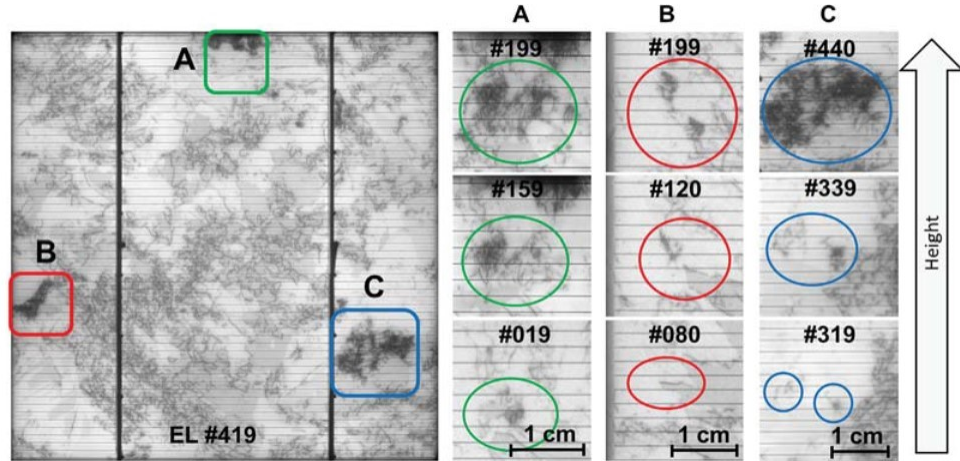


Figure 4.7: EL image of a polycrystalline solar cell(left) Focused images of three large defect clusters A, B, and C (right). From [21]

#### 4.2.5 Fabrication Shunts

Ohmic shunts are alternative current paths educes the amount of current flowing through the solar cell junction and thus the available voltage and current in the device. Shunts can be categorized by their origin as their signatures vary greatly based on imaging and cell type. Fabrication induced shunts often occur due to errors during the production process such as residue of the emitter at the edge of cells, scratches, and below grid lines [23].

The thermography image in Fig. 4.8 showcases heating at the outer edges indicative of an edge shunt. Edge shunts are typically caused by separation of the emitter from the rear

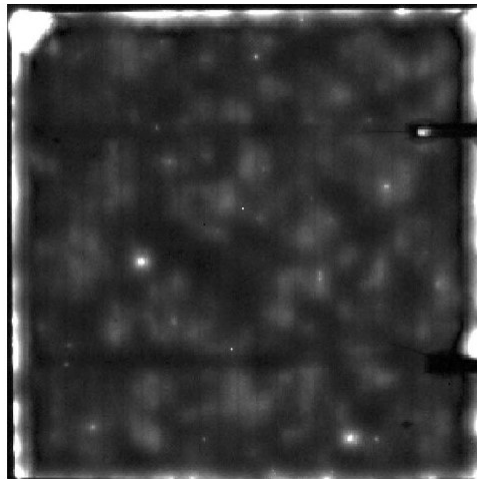


Figure 4.8: Lock-in thermogram of a 10x10 cm sq multicrystalline silicon solar cell under forward bias. Edge shunt mostly visible in the upper right hand region. From [22]

contact particularly harmful in that they leak current, lowering the overall power potential of the device. In earlier solar technologies, linear edge shunts were the dominant type, exhibiting linear IV characteristics, however edge isolation technologies have mostly phased out this type of defect [23]. However, non linear edge shunt such as those in Fig. 4.8 can also function as recombination sites where the emitter crosses the device surface. This technique is useful in imaging shunts to show heating where current collection occurs.

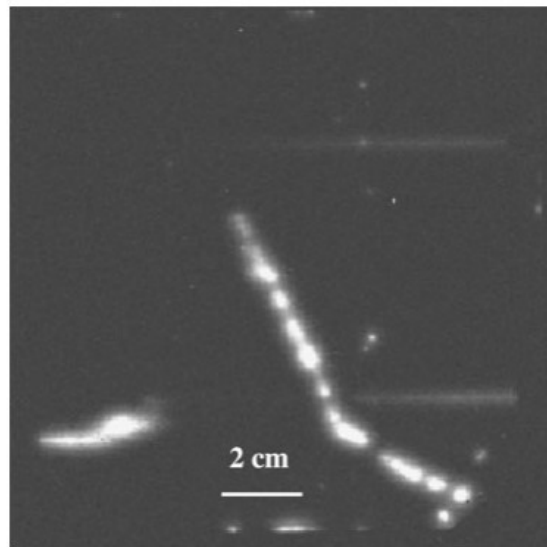


Figure 4.9: Lock-in thermogram of a similar multicrystalline silicon cell with two scratches that induced shunts. From [23]

Scratches, cracks, and holes, such as those portrayed in Fig. 4.9 often occur during processing and handling of the device. The thermal signature in Fig. 4.9 suggests that the emitter has been brought to the surface with a high density of recombination centers. In this way, the scratch acts similarly to the previously described nonlinear edge shunt, yielding a diode-like IV characteristic [23].

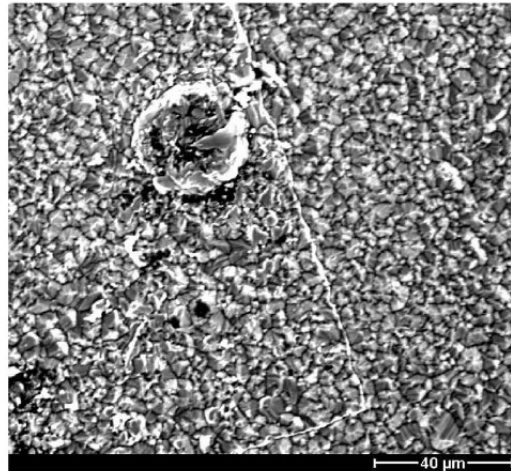


Figure 4.10: SEM image of a "hump" in the structure of a thin-film polycrystalline silicon cell on a substrate exhibiting shunting when covered by the emitter grid. From [22]

While thermal imaging techniques are useful in highlighting localized current collection, other imaging techniques can be useful in noting physical alterations to the device. Fig. 4.10 is an SEM image of a "hump" in a thin-film polycrystalline cell caused by incomplete emitter formation on an uneven substrate. This mechanism similarly induced shunting.

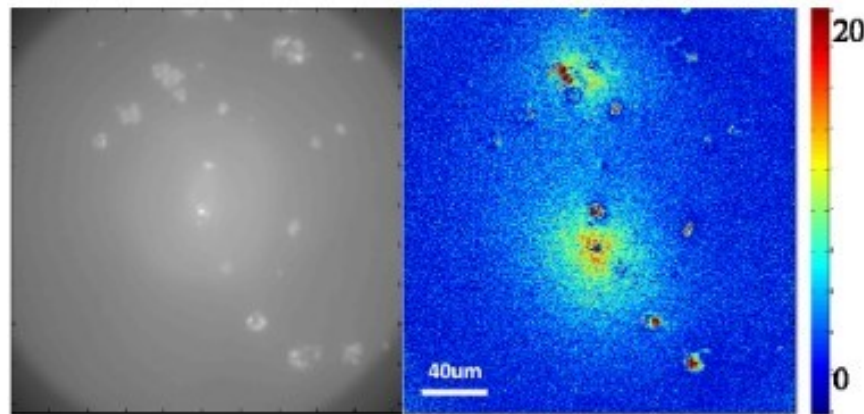


Figure 4.11: An EL image (left) and a thermal image (right) of linear ohmic shunts in a thin-film aluminum-silicon solar cell. From [24]

Fig. 4.11 represents another thermal manifestation of a linear shunt. When compared with the EL image on the left, the thermal image provides information concerning the heating and distribution of the shunt, indicated by the scale on the right from 0 to 20 K. These central shunts are similarly created during fabrication and can be due to an open emitter induced by stressing. The shunts could also be the result of the application of aluminum. Following application its precipitates could create regions of charged regions in the p-type material that could have formed an ohmic contact with the base and tunneled to contact the emitter [24].

#### 4.2.6 Material Shunts

Material-induced shunts are distinct as they manifest from the presence of strong recombination sites. While other defects located at grain boundaries, crystal clusters, or impurity precipitates invite recombination activity, they typically induce a trapped state as opposed to a shunt [23]. However, if their recombination current becomes strong enough, shunts can occur, presenting similarly to edge shunts.

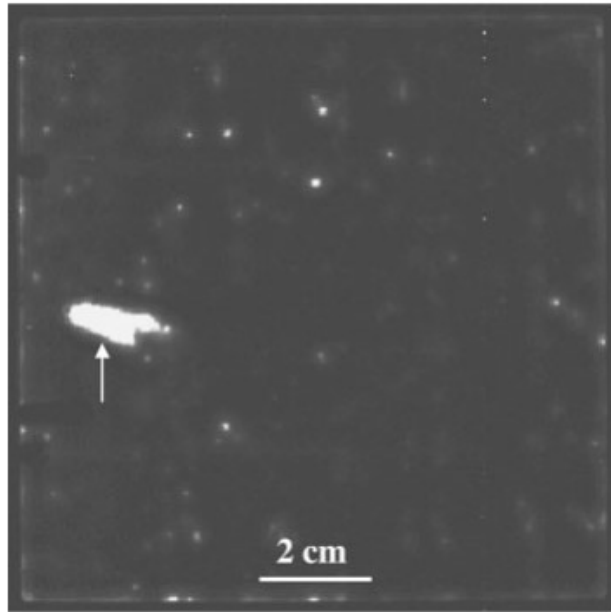


Figure 4.12: Lock-in thermogram of a multicrystalline silicon cell with shunting caused by an intrusion of Si<sub>3</sub>N<sub>4</sub>. From [23]

While thermography proves useful in identifying shunts, as many of them perform similarly, identifying their origins is less intuitive. Fig. 4.12 identifies a shunt due to the inclusion of nitrogen in the silicon likely from the crucible. The thermogram presents similarly to a linear or edge shunt as seen in Fig. 4.8 and Fig. 4.9. However, other investigations such as TEM and EDX showed that the cell contained nitrogen inclusions. It can be assumed that

recombination activity of interface states between Si and Si<sub>3</sub>N<sub>4</sub> material is responsible for the shunts [23].

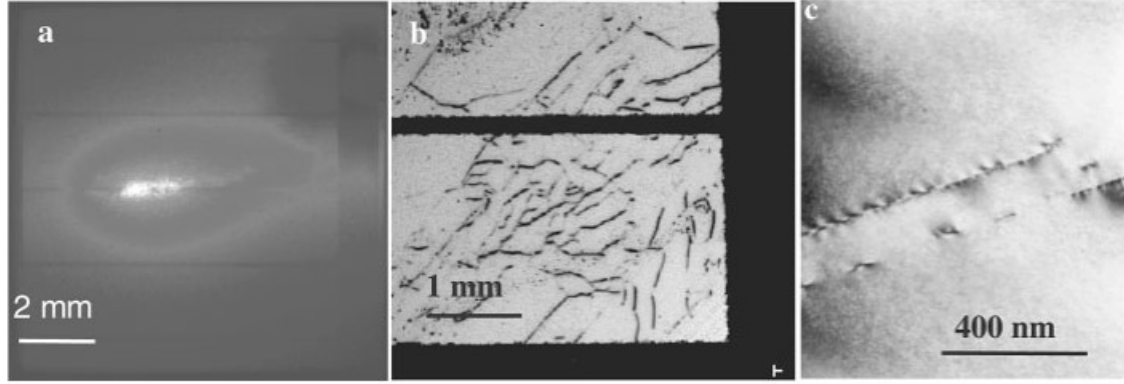


Figure 4.13: (a) Lock-in thermogram; (b) EBIC image; and (c) TEM image of a multicrystalline silicon cell shunting due to strongly recombinative crystal defects [23]

Fig. 4.13 shows three imaging techniques used to image strongly recombinative crystal defects including shunting. Such defects are distinct as ordinary GBs are visible under LBIC and EBIC techniques, but their recombination activity does not induce shunting. However, the defect shown in Fig. 4.13 strongly recombines to form shunts as demonstrated thermally in (a). In (b), the crystal structure can be observed, and in (c) the GBs are visible [23]. Implementing this imaging technique that demonstrates several perspectives is useful in understanding how different defect signatures can represent one type of defect.

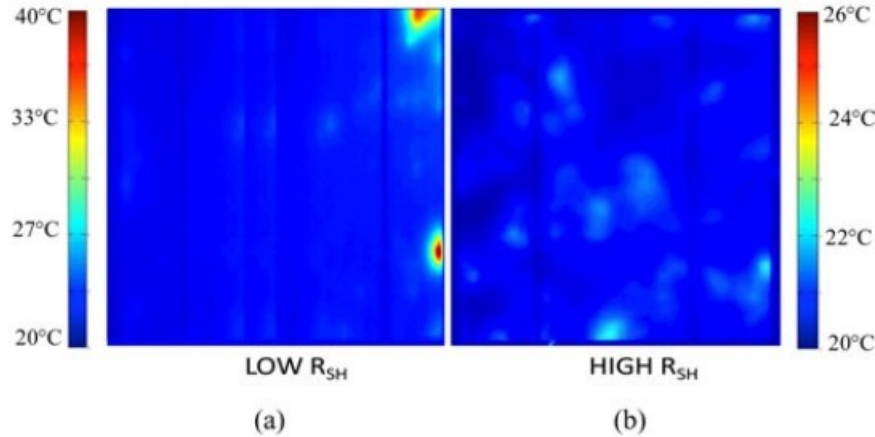


Figure 4.14: Thermography images of reverse biased multicrystalline cells under a periodically applied bias current of -1.6 A. The red spot in the upper right hand corner characterizes a local shunt (left) and the uniform temperature distribution signifies no shunting activity (right). From [25]

The thermal imaging in Fig. 4.14 displaying local shunting in the top and bottom right of the left cell. In multicrystalline cells, intragrain dislocations and impurity precipitates are typically responsible for current crowding that induces shunting activity, leading to local increases in temperature represented well through thermal imaging [25].

### 4.3 Defect prevention

Research has developed to identify methods to prevent the ills posed by defects in solar cells. Often referred to as defect passivation, techniques used at various points of the device manufacturing process aim to render defective material passive, or less affected by external stimuli. The initial techniques were developed in the 1990s for silicon cells, adding dielectric coatings such as silicon nitride or silicon dioxide for passivating defects on the surface of the cells [45]. Recently, the use of hydrogen has become much more common to account for surface defects as well as impurities, GBs, dislocations, and other point deep level defects. A frequent source comes in the form of a plasma enhanced chemical vapor introduced in the bulk dry fast firing process (around 700-800 degrees Celsius) in which cell contacts are formed [46].

In emergent technologies, defect passivation methods are similar, but must account for the different chemical structures of the cells. Commonly referred to as additive passivation, molecules that bond with point defect sites can be added at various stages of the fabrication process to prevent the development of defective mechanisms. In perovskite solar cells, surface defects are often passivated through the addition of metal cations or anions during doping processes to account for point interstitials and vacancies respectively. Similarly, the carrier transport layer is commonly doped with a variety of molecules to reduce nonradiative recombination mechanisms [45]. Finally, organic dyes often used for coloring textiles have recently been used in perovskites as additives due to their chemical and environmental stability. Their use produces more n-type films, improving charge carrier transport processes and decreases recombination pathways [46]. All of these methods have shown improvements in cell efficiencies and merit further development alongside emergent technologies.

# Chapter 5

## Progress and Conclusion

This chapter will outline the extent of the experimental work performed and compare its results to those found in the literature. Then conclusions can be made about defect formation and signatures in OPVs, and how they will continue to develop with further research.

### 5.1 Experimental data

#### 5.1.1 IV curves

To build upon previous work done by the lab, bulk *IV* curves were collected under light and dark conditions to evaluate cell performance, finding  $V_{OC}$  to determine the upper limit of voltage modulation prior to imaging. The cells were biased the a LabView program described in Chapter 3, measuring the current at 600 different voltage biases. The light conditions were provided by the Sunbrick solar simulator with an incoming power of 1 sun, described in Chapter 3. Fig. 5.1 displays an diode-like *IV* characteristic of an in-house cell taken by previous lab members, where Fig 5.2 shows an *IV* curve taken this year. The curves were taken from the same device three years apart. The discrepancies in quality of performance of the cells may be due to cell aging and exposure to the ambient, or inconsistencies in the quality of the contacts to the device.

It is worth mentioning that both *IV* characteristics showcase crossing between the light and dark measurements once the current remains positive. This effect is the result of a nonzero  $R_s$  and low  $R_{sh}$ , encouraging current leakage. These parasitic resistances are responsible for shunting activity described in the previous chapter.

#### 5.1.2 Thermorelectance images

The following TR images of in-house cells were taken from previous investigations to evaluate their similarities to those in the literature. As discussed in Chapter 3, the TR imaging algorithm produces a  $\Delta R/R$  and phase  $\Phi$  image that describe the TR amplitude and time

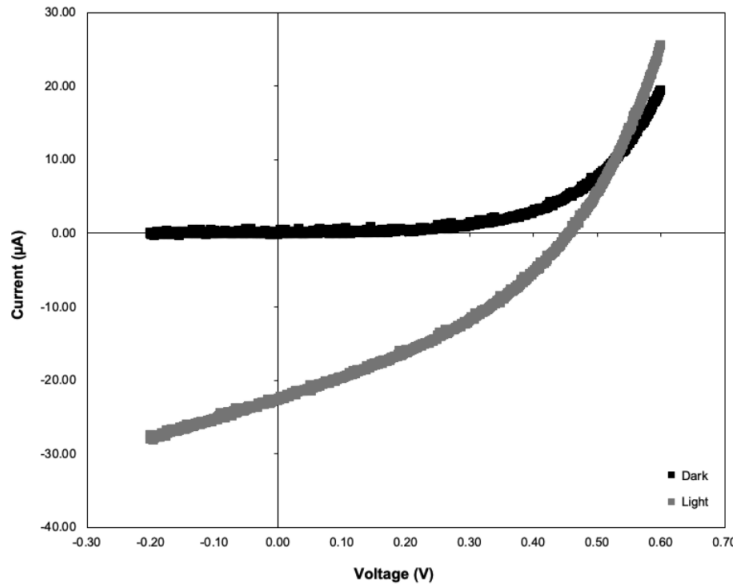


Figure 5.1: Bulk *IV* curve of an in-house fabricated device from 2019 using a solar simulator with incoming power  $100\text{mW}/\text{cm}^2$  under dark and light conditions. The graphed cell exhibits efficiencies up to  $\eta = 3\%$ .

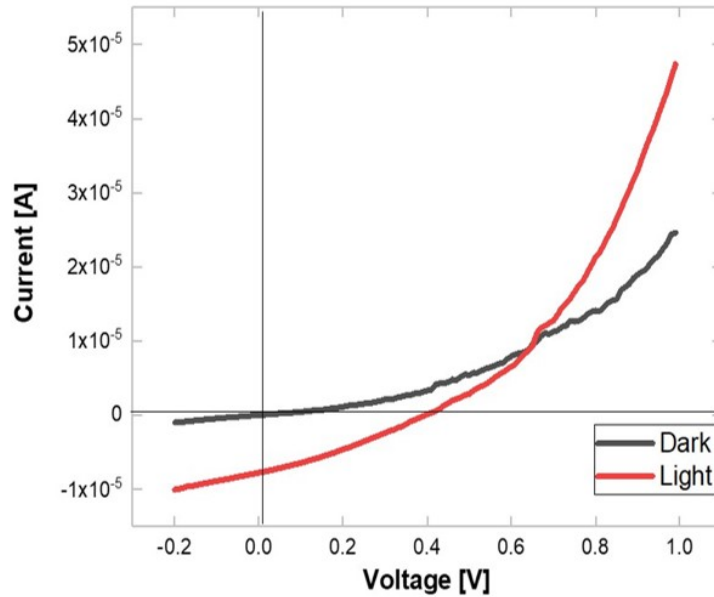


Figure 5.2: Bulk *IV* curve of an in-house fabricated device using a Sunbrick solar simulator with incoming power of 1 sun ( $1000\text{ W/m}^2$ ) under dark and light conditions. The cell exhibits efficiencies  $\eta = 0.02 - 3\%$ .

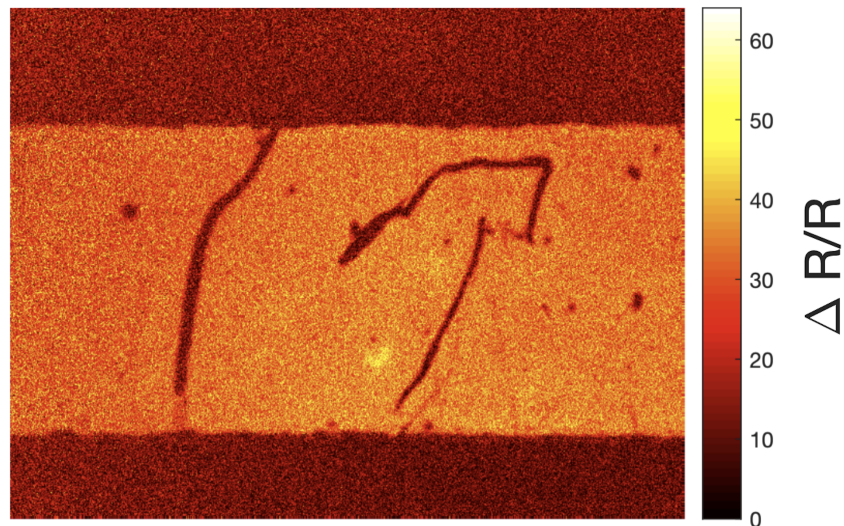
delay of the heat spread, respectively. The cells were biased with a sinusoidal voltage modulation between 0 and  $1.75 V_{OC}$  with  $V_{OC} = 0.375$ , which can be viewed in Fig. 5.3. The strip through the center of the images represent the biased cell opposed to the darker inactive substrate. The appearance of a hot spot exclusively in the  $\Delta R/R$  image signals that the defect and visible scratches are present in an electrically inactive portion of the shell and are not inducing shunting activity typically represented by images such as in Fig. 4.11.

Fig. 5.4 (a) shows a zoomed in portion of the active region of an in-house cell demonstrating a circular hot spot. The radial heat spreading exhibited in this cell is analogous to defects viewed in silicon solar cells such as Fig. 4.11 and Fig. 5.5. When this defect is paired with previous the analysis of squared voltage modulation amplitude in (b) and the radial distance from  $\Delta R/R$ , it can be understood that shunting is occurring from the existence of regions of lower resistance. As this defect scales linearly with the squared voltage modulation amplitude, it can be assumed that the electrical contacts are not influencing the signal. Thus, the region of lower resistance causing the defect could be due to impurities from the ambient or imprecise layering during device fabrication causing an open emitter.

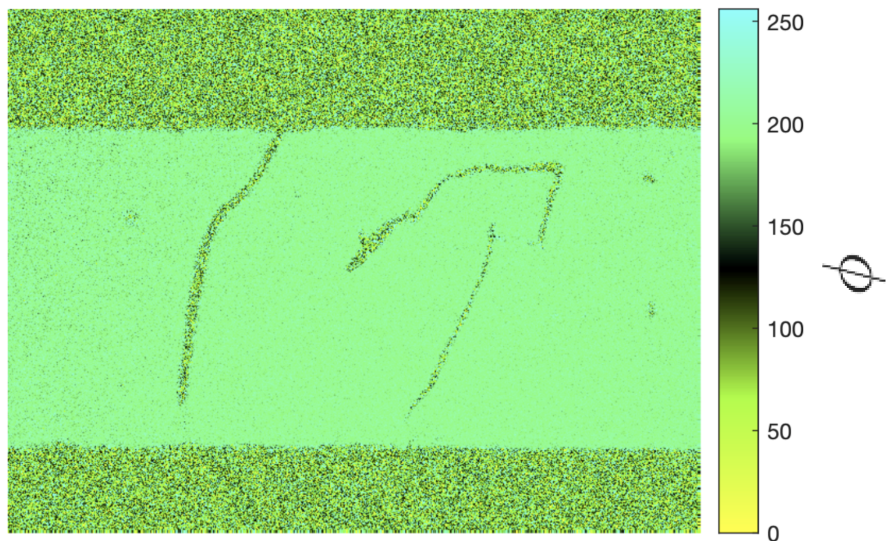
The defect displayed in Fig. 5.6 is similarly circular to Fig. 5.4, however the pattern spreads into concentric circles rather than an even radial pattern, signifying that the stronger TR signal may not be due to heating caused by a shunt. These circles are quantitatively represented in Fig. 5.6 (b) at one frequency and (c) at multiple frequencies, with the thermal signature decreasing with increasing radial distance. One would expect the signal to increase as frequency decreases as seen in Fig. 5.5, since the camera will have more time to image. However, the cell does not strongly respond with this relationship, emblematic of minimal dependence on modulation frequency. Thus, this defect must not lie within the active region, signifying that it may be due to a surface impurity such as oxygen, similar to Fig. 5.7 or photon emission as captured in Fig. 5.8.

## 5.2 Research progress

Overall, this project attempted to obtain TR images of in-house fabricated cells and compare their defect signatures to those presenting similarly in the literature. The experimental component of this investigation fell short as either the contacts of the device were inconsistent or the age of the device itself was operating at unpredictably. Similarly, our somewhat limited imaging approach of TR imaging and localized *IV* curves provided a narrow scope that did not encompass the potential range of defects the device could present. However, similarities were found in the origins and presentation of fabrication and materially induced shunt defects in silicon cells. The literature review conducted provided a thorough presentation of previous characterized defects in both older generations of solar cells and emergent technologies in an attempt to understand previous TR images taken by the lab. Defects can be understood through their origin and their degree of damage to the cell's structure and optoelectronic properties. Defect signatures similarly vary based on cell type and imaging methods that often characterize different components of device performance. Thus, future investigations should encompass a suite of imaging techniques and a more thorough understanding of



(a) Full cell  $\Delta R/R$  image of a hot spot accompanied by three scratches in the active region



(b) Phase image  $\Phi$  of the same region as (a) presenting three scratch defects

Figure 5.3: TR amplitude  $\Delta R/R$  (a) and (b) phase  $\Phi$  of a hot spot and three scratches in the active region of an in-house fabricated cell taken by previous Hudgings lab students [16]

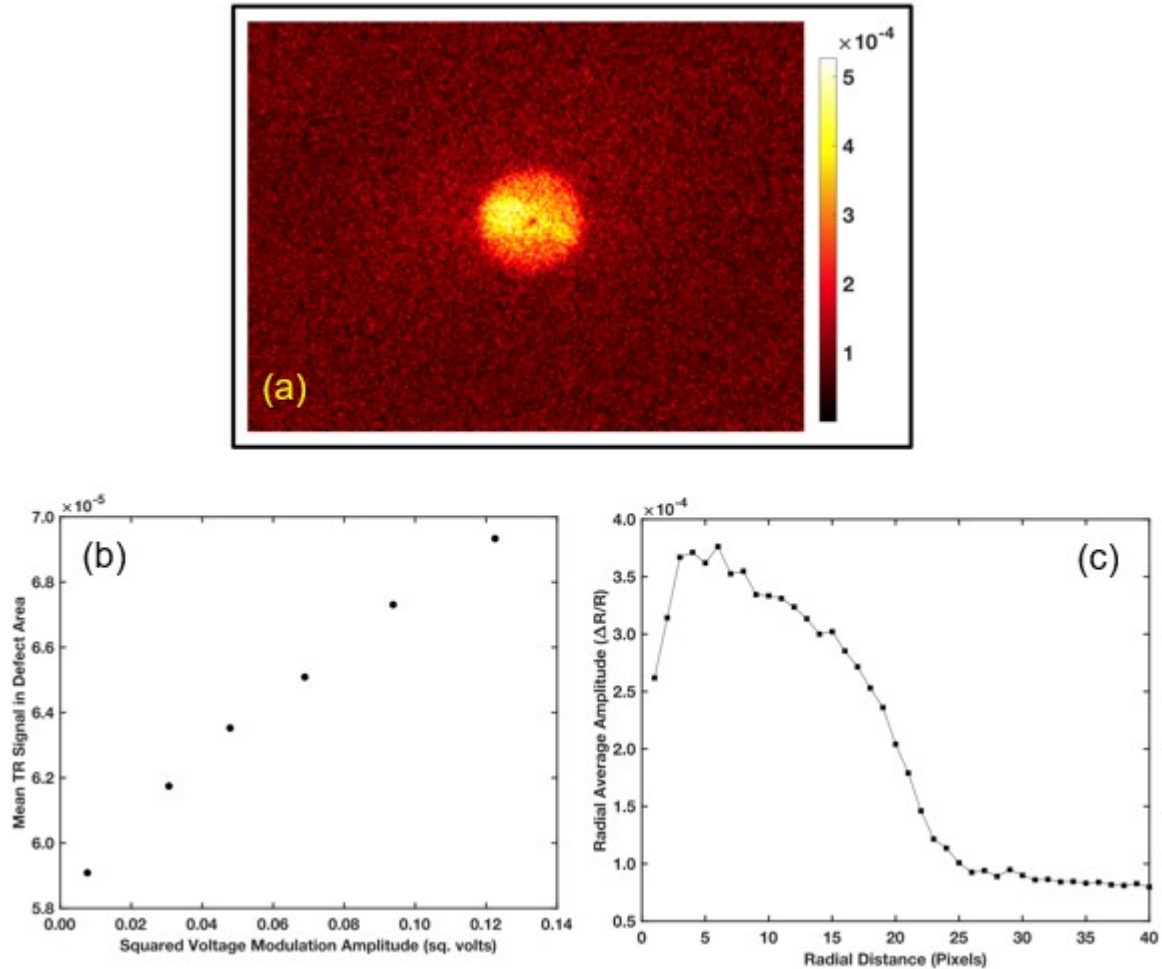


Figure 5.4: (a)  $\Delta R/R$  image of a radially symmetric hot spot in the active region of in-house fabricated cell (b)  $\Delta R/R$  plotted against squared voltage modulation amplitude [ $\Delta V^2$ ] of the hot spot in (a) demonstrating a linear relationship. (c)  $\Delta R/R$  plotted against the radial distance in pixels demonstrating heat spreading radially away from the center of the defect. Taken by previous Hudgings lab students. [7]

the cell chemistry, recombination structures, and fabrication methods to better understand potential defects.

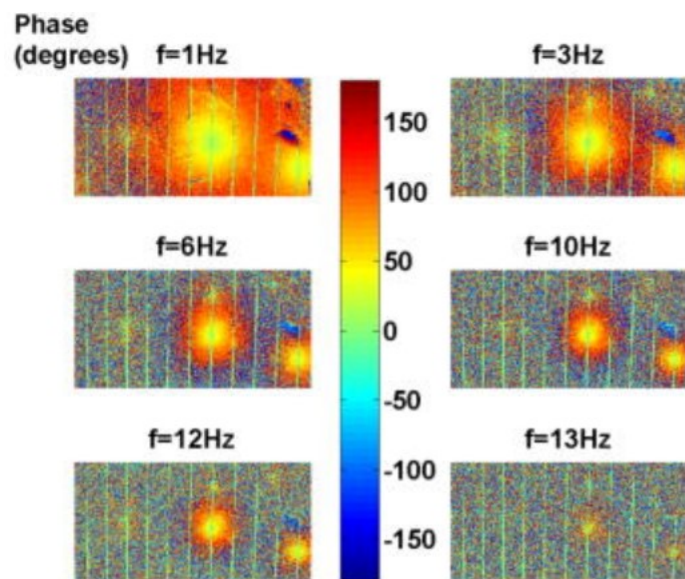


Figure 5.5: Radial hot spots in a silicon solar cell that scale inversely with modulation frequency. Shunts were cited to be caused by an open emitter from fabrication errors. [26]

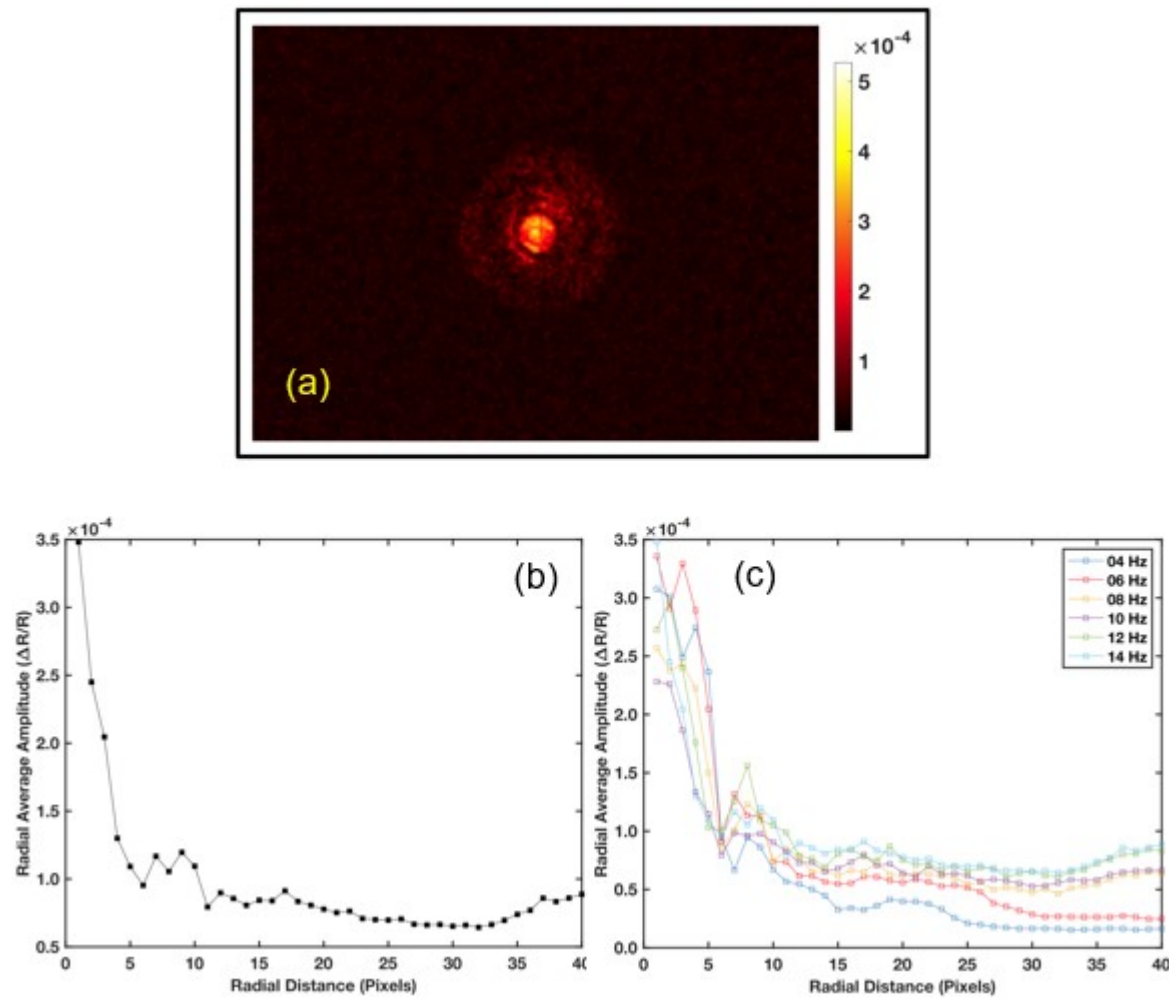


Figure 5.6: (a)  $\Delta R/R$  image of an in-house fabricated cell with a defect signature comprised of concentric rings, (b) and (c) present plots of  $\Delta R/R$  against radial distance, demonstrating the decreasing thermal signature as the radial distance increases. Taken by previous Hudgings lab students.[7]

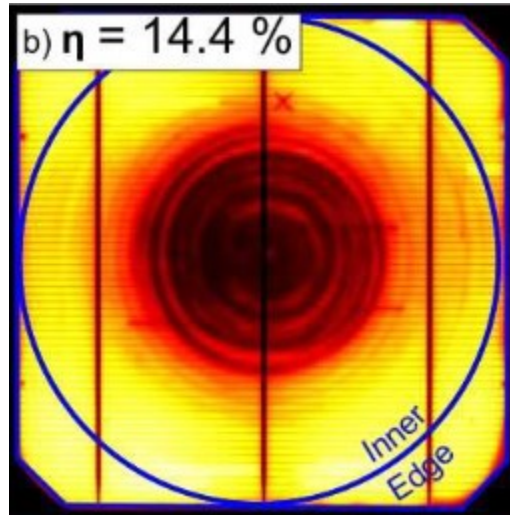


Figure 5.7: Photoluminescence image of a concentric ring defect on Czochralski-grown silicon wafers. Further imaging revealed the presence of oxygen impurities on the cell surface.[27]

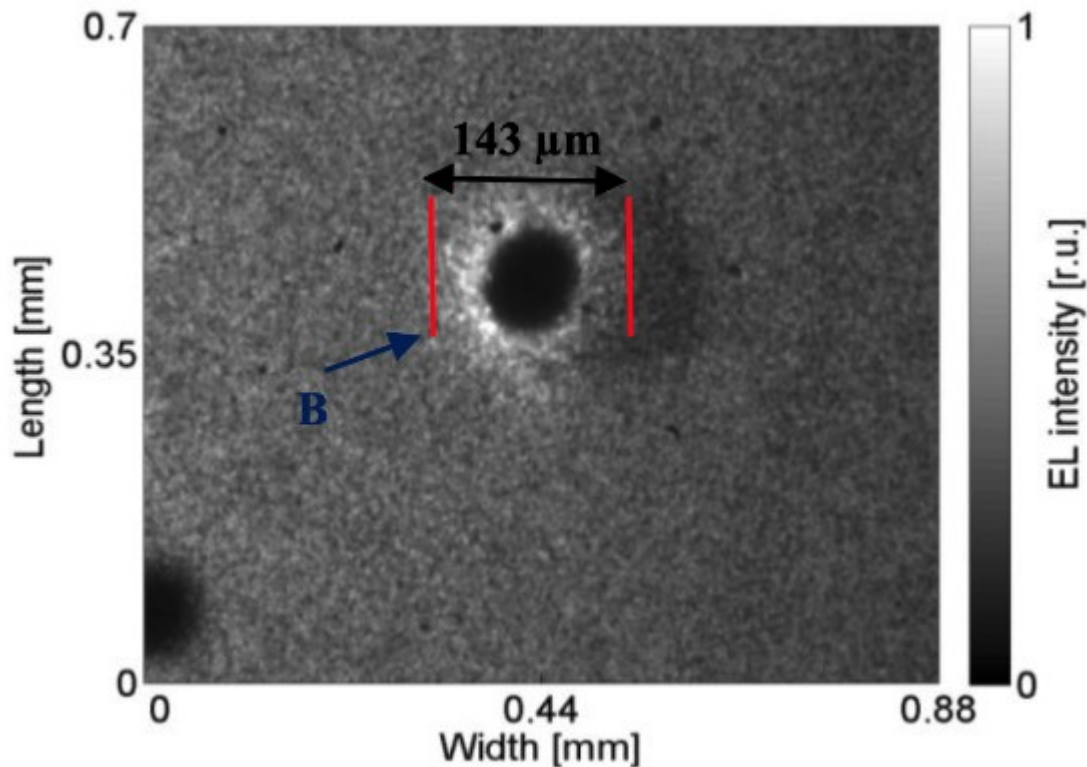


Figure 5.8: Electroluminescence image of a ring or "doughnut" defect on Copper indium gallium selenide cell. This imaging method measures the luminescence of the cell, demonstrating a recombinative defect as a result in photon emission. [28]

### 5.3 Future of OPVs

Further understanding of defect mechanisms in OPVs are needed to improve device performance for the mass market. Still, this research provides promising direction for OPVs as many of the defects plaguing solar cells are exclusive to older generations. Expanding defect characterization methods with OPVs and other promising emergent technologies such as perovskites is a useful direction for future research that would effectively promote device advancement as the search and demand for alternative energy sources continues.

# Bibliography

- [1] *Best Research-Cell Efficiency Chart*, URL <https://www.nrel.gov/pv/cell-efficiency.html>.
- [2] *Monocrystalline Silicon Cell - an overview | ScienceDirect Topics*, URL <https://www.sciencedirect.com/topics/engineering/monocrystalline-silicon-cell>.
- [3] *Si Wafer - an overview | ScienceDirect Topics*, URL <https://www.sciencedirect.com/topics/engineering/si-wafer>.
- [4] *Energy Bands - Definition and Classification of Energy Bands | Band Theory* (2019), URL <https://byjus.com/physics/what-are-energy-bands/>.
- [5] *Formation of a PN-Junction | PVEducation*, URL <https://www.pveducation.org/pvcdrrom/pn-junctions/formation-of-a-pn-junction>.
- [6] *2.6: The P-N Junction* (2018), URL
- [7] Alfred Molina, Ph.D. thesis, Pomona College, Claremont, CA (2021).
- [8] *Organic Photovoltaics Research | Department of Energy*, URL <https://www.energy.gov/eere/solar/organic-photovoltaics-research>.
- [9] Sabina Li, Ph.D. thesis, Pomona College, Claremont, CA (2017).
- [10] *Figure 2. Fluorescence microscopy of two poly-Si solar cells; on the...*, URL <https://www.researchgate.net/figure/Fluorescence-microscopy-of-two-poly-Si-solar-cells-10212003529>
- [11] *Elektrolumineszenz Inspektionssystem - MBJ Solutions GmbH* (2023), URL <https://www.mbj-solutions.com/>.
- [12] *Photoluminescence Imaging for Photovoltaic Applications | Elsevier Enhanced Reader*, URL <https://reader.elsevier.com/reader/sd/pii/S1876610212003529?token=B82B5EA6631E9A>
- [13] G. C. Ngo and E. Q. B. Macabebe, in *TENCON 2018 - 2018 IEEE Region 10 Conference* (2018), pp. 1479–1483, iSSN: 2159-3450.
- [14] *Light Beam Induced Current (LBIC) - Freiberg Instruments - life-time, single crystal orientation, PID, automation and more*, URL <https://www.freiberginstruments.com/upcdmdp/applications/light-beam-induced-current-life-time-single-crystal-orientation-pid-automation-and-more>

- [15] M. Kasemann, W. Kwapis, B. Walter, J. Giesecke, B. Michl, A. Schütt, J. Carstensen, S. Kluska, F. Granek, H. Kampwerth, et al., p. 9 (2008).
- [16] Valerie Wang, Ph.D. thesis, Pomona College, Claremont, CA (2020).
- [17] *High spatial resolution characterization of silicon solar cells using thermoreflectance imaging: Journal of Applied Physics: Vol 110, No 5*, URL <https://aip-scitation-org.ccl.idm.oclc.org/doi/10.1063/1.3629979>.
- [18] C. Ran, J. Xu, W. Gao, C. Huang, and S. Dou, Chemical Society Reviews **47**, 4581 (2018), ISSN 1460-4744, publisher: The Royal Society of Chemistry, URL <https://pubs.rsc.org/en/content/articlelanding/2018/cs/c7cs00868f>.
- [19] J. Huang, S. Yuan, X. Yu, and D. Yang, physica status solidi (a) **n/a**, 2200448 (????), ISSN 1862-6319, eprint: <https://onlinelibrary.wiley.com/doi/pdf/10.1002/pssa.202200448>, URL <https://onlinelibrary.wiley.com/doi/abs/10.1002/pssa.202200448>.
- [20] U. Hess, P. Y. Pichon, S. Seren, A. Schonecker, and G. Hahn, Solar Energy Materials and Solar Cells **117**, 471 (2013), ISSN 0927-0248, place: Amsterdam Publisher: Elsevier WOS:000325188400071, URL <https://linkinghub.elsevier.com/retrieve/pii/S0927024813003656>.
- [21] D. Kohler, A. Zuschlag, and G. Hahn, Solar Energy Materials and Solar Cells **120**, 275 (2014), ISSN 0927-0248, patent Number: A Place: Amsterdam Publisher: Elsevier Science Bv WOS:000329595400036, URL <https://linkinghub.elsevier.com/retrieve/pii/S092702481300487X>.
- [22] M. Langenkamp and O. Breitenstein, Solar Energy Materials and Solar Cells **72**, 433 (2002), ISSN 0927-0248, URL <https://www.sciencedirect.com/science/article/pii/S092702480100191X>.
- [23] O. Breitenstein, J. P. Rakotonaina, M. H. Al Rifai, and M. Werner, Progress in Photovoltaics: Research and Applications **12**, 529 (2004), ISSN 1099-159X, eprint: <https://onlinelibrary.wiley.com/doi/pdf/10.1002/pip.544>, URL <https://onlinelibrary.wiley.com/doi/abs/10.1002/pip.544>.
- [24] D. Kendig, G. B. Alers, and A. Shakouri, in *2010 IEEE International Reliability Physics Symposium* (2010), pp. 499–502, iSSN: 1938-1891.
- [25] D. Giaffreda, P. Magnone, M. Meneghini, M. Barbato, G. Meneghesso, E. Zanoni, E. Sangiorgi, and C. Fiegna, IEEE Journal of Photovoltaics **4**, 40 (2014), ISSN 2156-3403, conference Name: IEEE Journal of Photovoltaics.
- [26] Q. Zhou, X. Hu, K. Al-Hemyari, K. McCarthy, L. Domash, and J. A. Hudgings, Journal of Applied Physics **110**, 053108 (2011), ISSN 0021-8979, URL <https://doi.org/10.1063/1.3629979>.

- [27] J. Haunschmid, I. E. Reis, J. Geilker, and S. Rein, physica status solidi (RRL) – Rapid Research Letters **5**, 199 (2011), ISSN 1862-6270, eprint: <https://onlinelibrary.wiley.com/doi/pdf/10.1002/pssr.201105183>, URL <https://onlinelibrary.wiley.com/doi/abs/10.1002/pssr.201105183>.
- [28] J. Ramanujam and U. P. Singh, Energy & Environmental Science **10**, 1306 (2017), ISSN 1754-5706, publisher: The Royal Society of Chemistry, URL <https://pubs.rsc.org/en/content/articlelanding/2017/ee/c7ee00826k>.
- [29] J. C. Bernède, Journal of the Chilean Chemical Society **53**, 1549 (2008), ISSN 0717-9707, publisher: Sociedad Chilena de Química, URL [http://www.scielo.cl/scielo.php?script=sci\\_abstract&pid=S0717-97072008000300001&lng=es&nrm=isot&lng=en](http://www.scielo.cl/scielo.php?script=sci_abstract&pid=S0717-97072008000300001&lng=es&nrm=isot&lng=en).
- [30] M. A. Green, Progress in Photovoltaics: Research and Applications **13**, 447 (2005), ISSN 1099-159X, eprint: <https://onlinelibrary.wiley.com/doi/pdf/10.1002/pip.612>, URL <https://onlinelibrary.wiley.com/doi/abs/10.1002/pip.612>.
- [31] A. A. Bayod-Rújula, in *Solar Hydrogen Production*, edited by F. Calise, M. D'Accadia, M. Santarelli, A. Lanzini, and D. Ferrero (Academic Press, 2019), pp. 237–295, ISBN 978-0-12-814853-2, URL <https://www.sciencedirect.com/science/article/pii/B9780128148532000084>.
- [32] J. Nelson, *The Physics of Solar Cells* (PUBLISHED BY IMPERIAL COLLEGE PRESS AND DISTRIBUTED BY WORLD SCIENTIFIC PUBLISHING CO., 2003), ISBN 978-1-86094-340-9 978-1-84816-126-9, URL <https://www.worldscientific.com/worldscibooks/10.1142/p276>.
- [33] S. Bello, A. Urwick, F. Bastianini, A. J. Nedoma, and A. Dunbar, Energy Reports **8**, 89 (2022), ISSN 2352-4847, URL <https://www.sciencedirect.com/science/article/pii/S2352484722016493>.
- [34] T. Dittrich, *Materials Concepts for Solar Cells* (WORLD SCIENTIFIC (EUROPE), 2018), 2nd ed., ISBN 978-1-78634-448-9 978-1-78634-449-6, URL <https://www.worldscientific.com/worldscibooks/10.1142/q0131>.
- [35]
- [36] *LED Solar Simulator | sunbrick AAA Large Area Solar Simulator*, URL <https://g2voptics.com/products/sunbrick-solar-simulator/>.
- [37] *Figure 2. Fluorescence microscopy of two poly-Si solar cells; on the...*, URL <https://www.researchgate.net/figure/Fluorescence-microscopy-of-two-poly-Si-solar-cells-1000x1000px>

- [38] O. Breitenstein, J. Bauer, T. Trupke, and R. A. Bardos, Progress in Photovoltaics: Research and Applications **16**, 325 (2008), ISSN 1099-159X, eprint: <https://onlinelibrary.wiley.com/doi/pdf/10.1002/pip.803>, URL <https://onlinelibrary.wiley.com/doi/abs/10.1002/pip.803>.
- [39] G. Coletti, R. Kvande, V. D. Mihailetschi, L. J. Geerligs, L. Arnberg, and E. J. Øvreliid, Journal of Applied Physics **104**, 104913 (2008), ISSN 0021-8979, publisher: American Institute of Physics, URL <https://aip.scitation.org/doi/10.1063/1.3021355>.
- [40] T. Rachow, N. Milenkovic, B. Steinhauser, J. Benick, S. Janz, M. Hermle, and S. Reber, Energy Procedia **77**, 540 (2015), ISSN 1876-6102, URL <https://www.sciencedirect.com/science/article/pii/S1876610215008450>.
- [41] T. Hou, F. Liu, Z. Wang, Y. Zhang, Q. Wei, B. Li, S. Zhang, and G. Xing, Advanced Optical Materials **6**, 1800027 (2018), ISSN 2195-1071, eprint: <https://onlinelibrary.wiley.com/doi/pdf/10.1002/adom.201800027>, URL <https://onlinelibrary.wiley.com/doi/abs/10.1002/adom.201800027>.
- [42] A. Weu, J. A. Kress, F. Paulus, D. Becker-Koch, V. Lami, A. A. Bakulin, and Y. Vaynzof, ACS Applied Energy Materials **2**, 1943 (2019), publisher: American Chemical Society, URL <https://doi.org/10.1021/acsaem.8b02049>.
- [43] A.-F. Castro-Méndez, J. Hidalgo, and J.-P. Correa-Baena, Advanced Energy Materials **9**, 1901489 (2019), ISSN 1614-6840, eprint: <https://onlinelibrary.wiley.com/doi/pdf/10.1002/aenm.201901489>, URL <https://onlinelibrary.wiley.com/doi/abs/10.1002/aenm.201901489>.
- [44] W. Ming, D. Yang, T. Li, L. Zhang, and M. Du, Advanced Science **5**, 1700662 (2017), ISSN 2198-3844, URL <https://www.ncbi.nlm.nih.gov/pmc/articles/PMC5827569/>.
- [45] F. Gao, Y. Zhao, X. Zhang, and J. You, Advanced Energy Materials **10**, 1902650 (2020), ISSN 1614-6840, eprint: <https://onlinelibrary.wiley.com/doi/pdf/10.1002/aenm.201902650>, URL <https://onlinelibrary.wiley.com/doi/abs/10.1002/aenm.201902650>.
- [46] C. Sun, W. Weigand, J. Shi, Z. Yu, R. Basnet, S. P. Phang, Z. C. Holman, and D. Macdonald, Applied Physics Letters **115**, 252103 (2019), ISSN 0003-6951, publisher: American Institute of Physics, URL <https://aip.scitation.org/doi/full/10.1063/1.5132368>.